The Interplay of Excitonic Delocalization and Vibrational Localization in Optical Lineshapes: A variational polaron approach

Mike Reppert,[1, a)] Rajesh Dutta, and Lyudmila Slipchenko
Purdue University, Department of Chemistry, West Lafayette, IN 47920

(Dated: 3 February 2025)

The dynamics of molecular excitonic systems are complicated by a competition between electronic coupling (which drives delocalization) and vibrational-electronic (vibronic) interactions (which tend to encourage electronic localization). A particular challenge of molecular systems is that they typically possess a large number of independent vibrations, with frequencies often spanning the entire spectrum of relevant electronic energy gaps. Recent spectroscopic observations and numerical simulations on a water-soluble chlorophyll-binding protein (WSCP) reveal a transition between two regimes of vibronic behavior, a Redfield-like regime in which low-frequency vibrations respond to a delocalized excitonic state, and a Förster-like regime where high-frequency vibrations act as incoherent excitations on individual pigments. Although numerical simulations can reproduce these effects, there is a need for a simple, systematic theory that accurately describes the smooth transition between these two regimes in experimental spectra. Here we address this challenge by generalizing the variational polaron transform (VPT) approach of [E. Bloemsma, M. Silvis, A. Stradomska, and J. Knoester, *Chem. Phys.* 481, 250 (2016)] to include arbitrary bath densities for systems with or without symmetry. We benchmark this theory against both numerical matrix-diagonalization methods and experimental 77 K fluorescence spectra for two WSCP variants, obtaining quite satisfactory agreement in both cases. We apply this theory to offer an explanation for the large loss in apparent electronic coupling in the WSCP Q57K mutant and to examine the likely impact of the interplay between excitonic delocalization and vibrational localization on vibrational sideband shapes and apparent coupling strengths in high-resolution optical spectra for chlorophyll-protein complexes such as WSCP.

I. INTRODUCTION

Vibrational-electronic (vibronic) coupling plays a critical role in the spectroscopy and energy-transfer dynamics of molecular aggregates and pigment-protein complexes.[1–7] Depending on the parameter regime, vibration-induced modulation of inter-monomer energy gaps can either facilitate energy transport by catalyzing energy-transfer between non-resonant exciton states or induce localization through the disruption of coherent dynamics.[8] Yet the very diversity of roles played by vibronic coupling often complicates its characterization in any given physical system – a problem compounded by the often near-degeneracy of the relevant energy scales in molecular aggregates (e.g., static disorder, site-to-site coupling, vibrational frequencies, and vibronic reorganization energy).[7,9–12]

Theoretical approaches to this challenge typically center on either numerically exact (and computationally intensive) simulation methods or perturbative expansion in some physical parameter that is assumed to be small. For example, when site-to-site coupling is weak, incoherent Förster theory offers a useful description of energy transport in molecular systems.[13,14] In the opposite extreme, systems with weak vibronic coupling and strong site-to-site interacitons are amenable to Redfield theory and related second-order perturbation theories.[1,14] In the problematic "intermediate regime", methods such as the polaron transform (PT) and variational polaron transform (VPT) offer useful insight.[14,15]

One of the core challenges in testing and validating such theories is the difficulty of finding experimental molecular systems whose properties can be measured and tuned with sufficient precision to offer an "apples-to-apples" comparison of different coupling regimes. Most theoretical descriptions of molecular energy transfer and spectroscopic dynamics include enough free parameters – e.g., site energies, dipole orientations, vibrational spectral densities, and inter-molecular couplings – that it can be difficult to tell whether agreement with experiment indicates the accuracy of the theory or simply the flexibility of the procedure used to fit the model parameters.

In recent years, site-directed mutagenesis in pigment-protein complexes (PPCs) has emerged as one solution to this challenge.[7] By modifying specific protein side chains in the vicinity of protein-bound chlorophyll (Chl) molecules or related pigments, structure elements such as the local electrostatic and redox environment, hydrogen-bonding interactions, and steric strain can be systematically tuned, albeit with some care taken as to how closely the structure of the mutant protein matches expectations.[16–21] Recently, protein engineering methods have even progressed to the point that *de novo* proteins can be designed with sufficient precision to bind pigments in well-defined geometries.[22] On the one hand, such wet-lab tools offer a critical opportunity to test the quantum dynamics theories used to describe excitonic line shapes; on the other hand, theoretical and computational tools can offer important insight into the design and redesign of PPCs, not only through protein structure prediction

[a)] reppertm@purdue.edu

but also by "translating" such structural models into predicted optical and light-harvesting properties *before* going to the trouble of producing the complex experimentally.

In the specific context of vibronic coupling dynamics, a recent site-directed mutagenesis study in the water soluble chlorophyll protein (WSCP) of *Lepidium virginicum* (LvWSCP) revealed a pronounced variation in vibrational sideband (VSB) intensity as a function of excitonic delocalization across two interacting pigments.[23] Importantly, the observed effect was not uniform for all vibrational modes but instead was strongly frequency-dependent. Numerical simulations (in accordance with a recent analysis of the wild-type protein[24]) revealed that these changes are caused by a transition between a coherent Redfield-like regime, in which low-frequency vibrations respond to a delocalized excitation across both pigments, and an incoherent Förster-like regime, in which high-frequency vibrations appear as "dynamically localized" excitations of individual pigments.[7,24,25] Simulated spectra invoking only a mutation-induced loss of site-to-site electronic coupling was sufficient to describe the observed change in VSB intensity between wild-type (WT) and mutant spectra with near quantitative accuracy.

While such numerical simulations provide important insight, they can realistically be applied only to rather simple molecular systems and offer limited physical intuition. It is thus desirable to obtain a more intuitive and less numerically intensive approach to describing such effects, ideally with a well-defined relationship to the well-known Förster and Redfield limits. One such description can be obtained qualitatively by the *a priori* division of the vibrational spectral density into "high-frequency" and "low-frequency" components, to which different perturbative theories are applied separately.[25] Aside from its *ad hoc* justification, however, this approach is somewhat physically unsatisfying in that it lacks a mechanism for determining how the dividing line between "high" and "low" frequencies (which may vary from system to system) is to be determined. A more theoretically rigorous but practically limited approach is offered by the symmetry-adapted polaron transform theory of Bloemsma et al., which is applicable to systems of identical pigments with a single vibrational mode and identical vibronic coupling parameters at each site.[26] While the symmetry assumptions preclude this theory's quantitative application to most real experimental systems, it enjoys the distinct advantage of correctly predicting a continuous transition between Redfield-like delocalization for low-frequency modes and Förster-like localization of high-frequency vibrations. The key insight of this approach is to take advantage of the symmetry of the system by singling out a fully symmetric vibrational mode whose dynamics can be treated exactly through a full polaron transform. A VPT is then performed on the remaining (not fully symmetric) modes, which smoothly transition from coherent to incoherent dynamics as a function of the vibrational frequency.

The goal of this work is to develop a perturbative theory that combines the advantages of each of these approaches, correctly predicting frequency-dependent vibrational localization for systems with many vibrational modes and no symmetry constraints. Our central strategy is to follow the VPT approach of Bloemsma et al. as far as possible without imposing symmetry requirements. The key departure is to replace the fully symmetric mode of Bloemsma et al. (which does not exist in our asymmetric system) with the pure-dephasing component of the variationally transformed system-bath Hamiltonian, which, since it preserves the system eigenstates, can be treated analytically. The resulting theory smoothly interpolates between the Redfield and Förster limits without the need for symmetry constraints on the system properties. In spirit, this approach is very similar to Jang's recent polaron-transformed master equation method.[15] The primary distinction is that, after the polaron transformation is applied, we focus on the pure-dephasing dynamics that define absorption and fluorescence line shapes rather than on the energy transfer dynamics obtainable from the master equation.

This paper is organized as follows. Section II defines our theoretical model and derives absorption and fluorescence line shapes under the variational transform just described. Section III benchmarks this theory both against numerically exact simulations for model dimers and against experimental fluorescence data for the WSCP WT protein and Q57K mutants. Section IV closes with a discussion of the implication of these results for understanding experimental WSCP spectra and, more broadly, the interplay between excitonic delocalization and vibrational localization in PPCs and molecular aggregates.

II. THEORY

A. Model and Problem

We consider the composite Hamiltonian

$$\hat{H} = \hat{H}_{\mathrm{S}} + \hat{H}_{\mathrm{SB}} + \hat{H}_{\mathrm{B}}, \tag{1}$$

where

$$\hat{H}_{\mathrm{S}} = \sum_n \hbar\omega_n \left|n\right\rangle \left\langle n\right| + \sum_{m,n} \hbar V_{mn} \left|m\right\rangle \left\langle n\right| \tag{2}$$

represents the electronic energy of n interacting local sites (pigments),

$$\hat{H}_{\mathrm{B}} = \sum_k \hbar\Omega_k \hat{A}_k^\dagger \hat{A}_k \tag{3}$$

represents a harmonic thermal environment, and

$$\hat{H}_{\mathrm{SB}} = \sum_{n,k} \hbar g_{n,k} \left(\hat{A}_k^\dagger + \hat{A}_k\right) \left|n\right\rangle \left\langle n\right| \tag{4}$$

gives the interaction energy between the two. The state $|n\rangle$ represents the local excited state of a single pigment n, with site energy $\hbar\omega_n$, while V_{nm} is the electronic coupling constant for interactions between sites m and n in units of frequency. The operators $\hat{A}_k$ and $\hat{A}_k^\dagger$ are the usual annihilation and creation operators for harmonic mode k with frequency Ω_k. The system-bath coupling parameter g_{nk} is connected by

$$s_{nk} = \frac{g_{nk}^2}{\Omega_k^2}. \tag{5}$$

to the Huang-Rhys factor s_{nk} representing the dimensionless displacement of bath mode k in the electronic excited state of pigment n.[27]

Our goal is to calculate the time-domain absorption and fluorescence functions[13]

$$\alpha(t) = Z_{\mathrm{B}}^{-1} \left\langle 0 \left| \mathrm{Tr}_{\mathrm{B}} \left\{ \left(e^{-\frac{i}{\hbar}\hat{H}t} \hat{\boldsymbol{\mu}} e^{\frac{i}{\hbar}\hat{H}t} \right) \cdot \hat{\boldsymbol{\mu}} e^{-\beta \hat{H}_{\mathrm{B}}} \right\} \right| 0 \right\rangle \tag{6}$$

$$\varepsilon(t) = Z_{\mathrm{e}}^{-1} \mathrm{Tr}_{\mathrm{S,B}} \left\{ \left(e^{\frac{i}{\hbar}\hat{H}t} \hat{\boldsymbol{\mu}} e^{-\frac{i}{\hbar}\hat{H}t} \right) \cdot \hat{\boldsymbol{\mu}} e^{-\beta \hat{H}} \right\}, \tag{7}$$

from which the absorption and fluorescence spectra are calculated as

$$\alpha(\omega) = \int_{-\infty}^{\infty} dt\ \alpha(t) e^{-i\omega t} \tag{8}$$

$$\varepsilon(\omega) = \int_{-\infty}^{\infty} dt\ \varepsilon(t) e^{-i\omega t}. \tag{9}$$

Here Z_{B} and Z_{e} are partition functions for the electronic ground- and excited-state manifolds, respectively, and

$$\hat{\boldsymbol{\mu}} = \sum_n \boldsymbol{\mu}^{(n)} \left(|n\rangle \langle 0| + |0\rangle \langle n| \right) \tag{10}$$

is the total system dipole operator, i.e., the sum of the local dipole operators for each site n in the system. Note that there are two distinctions between absorption and fluorescence operators: the signs on the exponentials and the equilibrium density matrix over which the bath average is calculated.[13] In absorption, the bath is averaged over the ground-state bath density operator $Z_{\mathrm{B}}^{-1} e^{-\beta \hat{H}_{\mathrm{B}}}$. In emission, the bath is averaged over the *total excited state* density matrix $Z_{\mathrm{e}}^{-1} e^{-\beta \hat{H}}$, reflecting that emission comes from the equilibrated excited-state manifold.

B. Variational Polaron Transformation

The concept behind the polaron transformation is to transform each operator to a frame of "dressed" states, where the vibrational wavefunction shifts with each different electronic state. The *variational* polaron transformation (VPT) is similar, but allows the magnitude of the shift to vary for each vibration.[14,15,28] That is, instead of being shifted by the full distance $\frac{g_{nk}}{\Omega_k}$ between the equilibrium positions of the ground and n^{th} excited state potentials, the vibrational basis is shifted only by the distance $\xi_k \frac{g_{nk}}{\Omega_k}$, where $0 \leq \xi_k \leq 1$. Adjusting the value of ξ_k allows the vibrational basis to be shifted for each mode independently so as to minimize what remains of the system-bath interaction in the new basis. Physically, this approach may be motivated by noting that high-frequency bath modes are able to respond to system excitations more quickly, leading to a larger shift of the optimal basis. Low-frequency vibrations, by contrast, may be unable to respond to system excitation on the time scale over which energy is transferred from one site to the next; in this case, the vibration "feels" only partial excitation of each site (via the local site contribution to the delocalized exciton) and thus undergoes less relaxation in response.

To achieve this transformation, we define a displacement operator

$$\hat{D} = e^{\sum_{n,k} z_{nk} \left(\hat{A}_k^\dagger - \hat{A}_k \right) |n\rangle\langle n|} \tag{11}$$

with

$$z_{nk} \equiv \frac{g_{nk}}{\Omega_k} \xi_k. \tag{12}$$

Typically, the actual valuse of the ξ_k coefficients are obtained through a variational optimization of the free energy (see Appendix C), although other functional forms can be chosen.[14,15,29] Under this transformation, the Hamiltonian terms become

$$\hat{D}\hat{H}_{\mathrm{S}}\hat{D}^\dagger = \sum_n \hbar\omega_n |n\rangle\langle n| + \sum_{m,n} \hbar V_{mn} \hat{\Delta}_{mn} |m\rangle\langle n| \tag{13}$$

$$\hat{D}\hat{H}_{\mathrm{B}}\hat{D}^\dagger = \sum_k \hbar\Omega_k \hat{A}_k^\dagger \hat{A}_k - \sum_{n,k} \hbar\Omega_k z_{nk} |n\rangle\langle n| \left(\hat{A}_k^\dagger + \hat{A}_k \right) + \sum_{n,k} \hbar\Omega_k z_{nk}^2 |n\rangle\langle n| \tag{14}$$

$$\hat{D}\hat{H}_{\mathrm{SB}}\hat{D}^\dagger = \sum_{n,k} \hbar g_{nk} \left(\hat{A}_k^\dagger + \hat{A}_k - 2z_{nk} \right) |n\rangle\langle n| \tag{15}$$

with

$$\hat{\Delta}_{mn} = e^{\sum_k (z_{mk} - z_{nk})\left(\hat{A}_k^\dagger - \hat{A}_k\right)}. \tag{16}$$

Regrouping terms amongst these various contributions allows us to write the total transformed Hamiltonian

$$\tilde{H} = \hat{D}\hat{H}\hat{D}^\dagger = \tilde{H}_{\rm S} + \tilde{H}_{\rm B} + \tilde{H}_{\rm SB} \tag{17}$$

with

$$\tilde{H}_{\rm S} = \sum_n \hbar\left(\omega_n - \lambda_n\right)|n\rangle\langle n| + \sum_{m,n} \hbar\tilde{V}_{mn}|m\rangle\langle n| \tag{18}$$

$$\tilde{H}_{\rm SB} = \sum_{n,k} \hbar\left(g_{nk} - \Omega_k z_{nK}\right)\left(\hat{A}_k^\dagger + \hat{A}_k\right)|n\rangle\langle n| + \sum_{m,n} \hbar V_{mn}\left(\hat{\Delta}_{mn} - \left\langle\hat{\Delta}_{mn}\right\rangle_{\rm B}\right)|m\rangle\langle n| \tag{19}$$

$$\tilde{H}_{\rm B} = \sum_k \hbar\Omega_k \hat{A}_k^\dagger \hat{A}_k. \tag{20}$$

where

$$\lambda_n = \sum_k \left(2g_{nk}z_{nk} - \Omega_k z_{nk}^2\right) \tag{21}$$

$$= \sum_k \frac{g_{nk}^2}{\Omega_k}\xi_k\left(2 - \xi_k\right) \tag{22}$$

is the (partial) reorganization energy, and

$$\tilde{V}_{mn} = \left\langle\hat{\Delta}_{mn}\right\rangle_{\rm B} V_{mn}. \tag{23}$$

Here we have both added and subtracted the bath averaged displacement operators (see Appendix A)

$$\left\langle\hat{\Delta}_{mn}\right\rangle_{\rm B} = \left\langle e^{\sum_k (z_{mk} - z_{nk})\left(\hat{A}_k^\dagger - \hat{A}_k\right)}\right\rangle_{\rm B} \tag{24}$$

$$= e^{-\sum_k \frac{\xi_k^2 (g_{mk} - g_{nk})^2}{2\Omega_k^2}(1 + 2\bar{n}(\Omega))} \tag{25}$$

so as to renormalize the coupling constants V_{mn} to account for bath reorganization, which tends to weaken inter-site coupling. In Eq. (25), the quantity

$$\bar{n}(\Omega) = \frac{1}{e^{\beta\hbar\Omega} - 1} \tag{26}$$

is the thermal occupation number.

The system-bath interaction Hamiltonian of Eq. (19) has two contributions: the first (which has been partially eliminated by the transformation) represents bath-induced fluctuations to the individual site energies, while the second term represents bath-induced fluctuations to the system couplings away from their bath-averaged values $\tilde{V}_{mn}$.

To calculate optical line shapes, we work in the $\tilde{H}_{\rm S}$ eigenbasis, i.e., with the states

$$|\mu\rangle = \sum_m u_{\mu m}|m\rangle, \tag{27}$$

where $u_{\mu m}$ are the matrix elements of the unitary transformation that diagonalizes $\tilde{H}_{\rm S}$. In what follows, Greek indices refer to this eigenbasis, while Latin indices refer to local system sites. In this basis, the Hamiltonian terms can be expressed as

$$\tilde{H}_{\rm S} = \sum_\mu \hbar\tilde{\omega}_\mu|\mu\rangle\langle\mu| \tag{28}$$

$$\tilde{H}_{\rm B} = \sum_k \hbar\Omega_k \hat{A}_k^\dagger \hat{A}_k \tag{29}$$

$$\tilde{H}_{\rm SB} = \sum_{\mu,\nu}\left(\hat{B}_{\mu\nu}^{(1)} + \hat{B}_{\mu\nu}^{(2)}\right)|\mu\rangle\langle\nu|, \tag{30}$$

with

$$\tilde{B}_{\mu\nu}^{(1)} = \hbar\sum_{n,k} u_{\mu n}u_{\nu n}\left(g_{nk} - \Omega_k z_{nK}\right)\left(\hat{A}_k^\dagger + \hat{A}_k\right) \tag{31}$$

$$\tilde{B}_{\mu\nu}^{(2)} = \hbar\sum_{m,n} u_{\mu m}u_{\nu n}V_{mn}\left(\hat{D}_{mm}\hat{D}_{nn}^\dagger - \left\langle\hat{\Delta}_{mn}\right\rangle_{\rm B}\right). \tag{32}$$

C. Emission Line Shape

The emission spectrum can be calculated by applying the partial polaron transformation to Eq. (7):

$$\varepsilon(t) = Z_{\rm e}^{-1}{\rm Tr}_{\rm S,B}\left\{e^{\frac{i}{\hbar}\tilde{H}t}\hat{D}\hat{\boldsymbol{\mu}}\hat{D}^\dagger e^{-\frac{i}{\hbar}\tilde{H}t}\hat{D}\hat{\boldsymbol{\mu}}\hat{D}^\dagger e^{-\beta\tilde{H}}\right\}. \tag{33}$$

To evaluate this expression, we introduce two approximations, both motivated by the results of Ref.[26] From $\tilde{H}_{\rm SB}$:

1. We drop $\tilde{B}_{\mu\nu}^{(2)}$ term entirely, and

2. We retain only the diagonal elements of $\tilde{B}_{\mu\nu}^{(1)}$.

The neglect of off-diagonal elements in both operators serves to eiminate energy relaxation (and thus lifetime broadening) between polaron states; our line shape formulas will thus operate within a pure-dephasing approximation in the polaron frame. The additional neglect of the diagonal elements of $\tilde{B}^{(2)}_{\mu\nu}$ is introduced for convenience in evaluating the analytical expressions, motivated by the observation of Ref.[26] that even the complete neglect of this perturbation provides physically reasonable line shapes in the full polaron limit.

Within these two approximations, the emission line shape can be evaluated analytically as

$$\varepsilon(t) = Z_{\rm e}^{-1} \sum_{\mu,\kappa,\lambda} \left(\boldsymbol{\mu}^{(\kappa)} \cdot \boldsymbol{\mu}^{(\lambda)}\right) e^{i\tilde{\omega}_\mu t - \beta\hbar\tilde{\omega}_\mu} {\rm Tr}_{\rm B} \left\{ e^{\frac{i}{\hbar}\left(\hat{H}_{\rm B}+\hat{B}^{(1)}_{\mu\mu}\right)t} \hat{D}_{\mu\kappa} e^{-\frac{i}{\hbar}\tilde{H}_{\rm B} t} \hat{D}^\dagger_{\lambda\mu} e^{-\beta\left(\tilde{H}_{\rm B}+\hat{B}^{(1)}_{\mu\mu}\right)} \right\}. \tag{34}$$

Here the excitonic dipoles are

$$\boldsymbol{\mu}^{(\kappa)} = \sum_n u_{\kappa n} \boldsymbol{\mu}^{(n)}. \tag{35}$$

The diagonal coupling elements

$$\hat{B}^{(1)}_{\mu\mu} = \hbar \sum_k g_{\mu k} \left(\hat{A}^\dagger_k + \hat{A}_k\right). \tag{36}$$

have the same form as the original (untransformed) $\tilde{H}_{\rm SB}$ with linear coupling coefficients

$$g_{\mu k} = (1-\xi_k) \sum_n u^2_{\mu n} g_{nk}. \tag{37}$$

They can thus be conveniently treated by defining a new displacement operator

$$\tilde{D} = e^{-\sum_{\mu,k} \frac{g_{\mu k}}{\Omega_k}\left(\hat{A}^\dagger_k - \hat{A}_k\right)|\mu\rangle\langle\mu|}, \tag{38}$$

which transforms the bath Hamiltonian as

$$\begin{aligned}\tilde{D}\hat{H}_{\rm B}\tilde{D}^\dagger = \hat{H}_{\rm B} &+ \sum_\mu \hat{B}^{(1)}_{\mu\mu} |\mu\rangle\langle\mu| \\ &+ \sum_{\mu,k} \hbar\Omega_k \frac{g^2_{\mu k}}{\Omega^2_k} |\mu\rangle\langle\mu|. \end{aligned} \tag{39}$$

Then

$$\begin{aligned}\varepsilon(t) = \frac{Z_B}{Z_{\rm e}} &\sum_{\mu,\kappa,\lambda} \left(\boldsymbol{\mu}^{(\kappa)} \cdot \boldsymbol{\mu}^{(\lambda)}\right) e^{i\omega_\mu t - \beta\hbar\omega_\mu} \\ &\times \left\langle e^{\frac{i}{\hbar}\hat{H}_{\rm B} t} \tilde{D}^\dagger_{\mu\mu} \hat{D}_{\mu\kappa} e^{-\frac{i}{\hbar}\tilde{H}_{\rm B} t} \hat{D}^\dagger_{\lambda\mu} \tilde{D}_{\mu\mu} \right\rangle_{\rm B}, \end{aligned} \tag{40}$$

where

$$\omega_\mu = \tilde{\omega}_\mu - \sum_k \frac{g^2_{\mu k}}{\Omega_k}. \tag{41}$$

Noting that

$$\hat{D}_{\mu\kappa} = \left\langle \mu \left| e^{\sum_{n,k} z_{nK}\left(\hat{A}^\dagger_k - \hat{A}_k\right)|n\rangle\langle n|} \right| \kappa \right\rangle \tag{42}$$

$$= \sum_{m,p} u_{\mu m} u_{\kappa p} \left\langle m \left| e^{\sum_{n,k} z_{nK}\left(\hat{A}^\dagger_k - \hat{A}_k\right)|n\rangle\langle n|} \right| p \right\rangle \tag{43}$$

$$= \sum_n u_{\mu n} u_{\kappa n} e^{\sum_k z_{nk}\left(\hat{A}^\dagger_k - \hat{A}_k\right)}. \tag{44}$$

and

$$\tilde{D}_{\mu\mu} = e^{-\sum_k \frac{g_{\mu k}}{\Omega_k}\left(\hat{A}^\dagger_k - \hat{A}_k\right)} \tag{45}$$

produces

$$\left\langle e^{\frac{i}{\hbar}\hat{H}_{\rm B} t} \tilde{D}^\dagger_{\mu\mu} \hat{D}_{\mu\kappa} e^{-\frac{i}{\hbar}\tilde{H}_{\rm B} t} \hat{D}^\dagger_{\lambda\mu} \tilde{D}_{\mu\mu} e^{-\beta\tilde{H}_{\rm B}} \right\rangle_{\rm B} \tag{46}$$

$$\begin{aligned}&= \sum_{n,m} u_{\mu n} u_{\kappa n} u_{\lambda m} u_{\mu m} \\ &\times \left\langle e^{\frac{i}{\hbar}\hat{H}_{\rm B} t} e^{\sum_k \left[\frac{g_{\mu k}}{\Omega_k} + z_{nk}\right]\left(\hat{A}^\dagger_k - \hat{A}_k\right)} e^{-\frac{i}{\hbar}\tilde{H}_{\rm B} t} \right. \\ &\qquad \left. \times\, e^{-\sum_k \left[z_{mk} + \frac{g_{\mu k}}{\Omega_k}\right]\left(\hat{A}^\dagger_k - \hat{A}_k\right)} \right\rangle_{\rm B}. \end{aligned} \tag{47}$$

Evaluation of the bath average is somewhat tedious. The result (see Appendix B) is

$$\begin{aligned}&\left\langle e^{\frac{i}{\hbar}\hat{H}_{\rm B} t} \tilde{D}^\dagger_{\mu\mu} \hat{D}_{\mu\kappa} e^{-\frac{i}{\hbar}\tilde{H}_{\rm B} t} \hat{D}^\dagger_{\lambda\mu} \tilde{D}_{\mu\mu} \right\rangle_{\rm B} \\ &= \sum_{n,m} u_{\mu n} u_{\kappa n} u_{\lambda m} u_{\mu m} e^{-\sum_k \frac{(z_{nk} - z_{mk})^2}{2}(1 + 2\bar{n}(\omega_k))} \\ &\qquad \times e^{G^{(mn)}_\mu(t) - G^{(mn)}_\mu(0)} \end{aligned} \tag{48}$$

with

$$\begin{aligned}G^{(mn)}_\mu(t) = \sum_k \frac{1}{\Omega^2_k} &\left[g_{nk} g_{mk} \xi^2_k + \xi_k \left(g_{mk} + g_{nk}\right) g_{\mu k} + g^2_{\mu k}\right] \\ &\times \left(e^{-i\Omega_k t} + 2\bar{n}(\Omega_k) \cos\Omega_k t\right) \end{aligned} \tag{49}$$

After substituting Eq. (48) into Eq. (40), the sums over κ and λ can be performed directly, using the fact that

$$\sum_{\kappa} u_{\kappa m}\boldsymbol{\mu}^{(\kappa)} = \sum_{\kappa} u_{\kappa m}\sum_{n} u_{\kappa n}\boldsymbol{\mu}^{(n)} = \sum_{n}\left(\sum_{\kappa} u_{\kappa m}u_{\kappa n}\right)\boldsymbol{\mu}^{(n)} = \boldsymbol{\mu}^{(m)}, \quad (50)$$

to obtain

$$\varepsilon(t) = \frac{Z_B}{Z_{\mathrm{e}}}\sum_{\mu} e^{i\omega_\mu t-\beta\hbar\omega_\mu}\sum_{n,m} u_{\mu n}u_{\mu m}\left(\boldsymbol{\mu}^{(n)}\cdot\boldsymbol{\mu}^{(m)}\right) \times e^{-\sum_k \xi_k^2\frac{(g_{nk}-g_{mk})^2}{2\Omega_k^2}(1+2\bar{n}(\Omega_k))}e^{G_\mu^{(mn)}(t)-G_\mu^{(mn)}(0)}. \quad (51)$$

D. Absorption Line Shape

The absorption line shape can similarly be evaluated as

$$\begin{aligned}
\alpha(t) &\approx Z_{\mathrm{B}}^{-1}\left\langle 0\left|\mathrm{Tr}_{\mathrm{B}}\left\{e^{-\frac{i}{\hbar}\hat{H}t}\hat{\boldsymbol{\mu}}e^{\frac{i}{\hbar}\hat{H}t}\hat{\boldsymbol{\mu}}e^{-\beta\hat{H}_{\mathrm{B}}}\right\}\right|0\right\rangle && (52)\\
&= \sum_{\kappa,\lambda}\left(\hat{\boldsymbol{\mu}}^{(\kappa)}\cdot\hat{\boldsymbol{\mu}}^{(\lambda)}\right)\left\langle e^{-\frac{i}{\hbar}\hat{H}_{\mathrm{B}}t}\left\langle\kappa\left|e^{\frac{i}{\hbar}\hat{H}t}\right|\lambda\right\rangle\right\rangle_{\mathrm{B}} && (53)\\
&\approx \sum_{\kappa,\lambda,\mu}\left(\hat{\boldsymbol{\mu}}^{(\kappa)}\cdot\hat{\boldsymbol{\mu}}^{(\lambda)}\right)e^{i\tilde{\omega}_\mu t}\times\left\langle e^{-\frac{i}{\hbar}\hat{H}_{\mathrm{B}}t}\hat{D}^\dagger_{\kappa\mu}e^{\frac{i}{\hbar}\left(\tilde{H}_{\mathrm{B}}+\tilde{B}^{(1)}_{\mu\mu}\right)t}\hat{D}_{\mu\lambda}\right\rangle_{\mathrm{B}} && (54)\\
&= \sum_{\kappa,\lambda,\mu}\left(\hat{\boldsymbol{\mu}}^{(\kappa)}\cdot\hat{\boldsymbol{\mu}}^{(\lambda)}\right)e^{i\tilde{\omega}_\mu t-i\sum_k\frac{g^2_{\mu k}}{\Omega_k}t}\times\left\langle e^{-\frac{i}{\hbar}\hat{H}_{\mathrm{B}}t}\hat{D}^\dagger_{\kappa\mu}\tilde{D}_{\mu\mu}e^{\frac{i}{\hbar}\hat{H}_{\mathrm{B}}t}\tilde{D}^\dagger_{\mu\mu}\hat{D}_{\mu\lambda}\right\rangle_{\mathrm{B}} && (55)
\end{aligned}$$

Using Eqs. (44) and (45) gives

$$\begin{aligned}
\alpha(t) &= \sum_{\kappa,\lambda,\mu}\left(\hat{\boldsymbol{\mu}}^{(\kappa)}\cdot\hat{\boldsymbol{\mu}}^{(\lambda)}\right)e^{i\omega_\mu t}\sum_{m,n}u_{\mu n}u_{\kappa n}u_{\mu m}u_{\lambda m}\\
&\times\left\langle e^{-\frac{i}{\hbar}\hat{H}_{\mathrm{B}}t}e^{-\sum_k\left[z_{nk}+\frac{g_{\mu k}}{\Omega_k}\right]\left(\hat{A}^\dagger_k-\hat{A}_k\right)}e^{\frac{i}{\hbar}\hat{H}_{\mathrm{B}}t}\right.\\
&\qquad\left.\times e^{+\sum_k\left[z_{mk}+\frac{g_{\mu k}}{\Omega_k}\right]\left(\hat{A}^\dagger_k-\hat{A}_k\right)}\right\rangle_{\mathrm{B}} && (56)\\
&= \sum_{\kappa,\lambda,\mu}\left(\hat{\boldsymbol{\mu}}^{(\kappa)}\cdot\hat{\boldsymbol{\mu}}^{(\lambda)}\right)e^{i\omega_\mu t}\sum_{m,n}u_{\mu n}u_{\kappa n}u_{\mu m}u_{\lambda m}\\
&\times e^{-\sum_k\frac{(z_{nk}-z_{mk})^2}{2}(1+2\bar{n}(\Omega_k))}e^{\bar{G}_\mu^{(mn)}(t)-G_\mu^{(mn)}(0)}, && (57)
\end{aligned}$$

following a procedure nearly identical to the one outlined above for $\varepsilon(t)$. Here $\bar{G}_\mu^{(mn)}(t)$ denotes the complex conjugate of $G_\mu^{(mn)}(t)$. Returning the dipole vectors to the site basis, we obtain

$$\alpha(t) = \sum_{\mu} e^{i\omega_\mu t}\sum_{m,n}\left(\boldsymbol{\mu}^{(n)}\cdot\boldsymbol{\mu}^{(m)}\right)u_{\mu n}u_{\mu m} \times e^{-\sum_k\frac{(z_{nk}-z_{mk})^2}{2}(1+2\bar{n}(\Omega_k))}e^{\bar{G}_\mu^{(mn)}(t)-G_\mu^{(mn)}(0)}. \quad (58)$$

E. Uncorrelated Baths

When each system site interacts with an independent thermal bath, the coupling coefficients g_{nk} are characterized by the condition $g_{nk}g_{mk} = 0$ whenever $m \neq n$. This simplifies the expression for the line shape function $G_\mu^{(mn)}(t)$ because it implies that

$$\begin{aligned}
g_{mk}g_{nk} &= g^2_{nk}\delta_{mn} && (59)\\
g_{nk}g_{\mu k} &= u^2_{\mu n}g^2_{nk}\left(1-\xi_k\right) && (60)\\
g^2_{\mu k} &= \sum_n u^4_{\mu n}g^2_{nk}\left(1-\xi\right)^2. && (61)
\end{aligned}$$

If we define site-specific weighting functions

$$\chi_n(\Omega) = \sum_k^{g_{nk}\neq 0}\xi_k\delta\left(\Omega-\Omega_k\right) \quad (62)$$

and spectral densities

$$\begin{aligned}
J_n(\Omega) &\equiv \sum_k\frac{g^2_{nk}}{\Omega^2_k}\delta\left(\Omega-\Omega_k\right) && (63)\\
J_\mu(\Omega) &\equiv \sum_n u^4_{\mu n}J_n(\Omega)\left(1-\chi_n(\Omega)\right)^2, && (64)
\end{aligned}$$

the line shape function can be written in terms of an effective spectral density

$$\begin{aligned}
J^{(mn)}_\mu(\Omega) &= \delta_{mn}J_n(\Omega)\chi^2_n(\Omega) + J_\mu(\Omega)\\
&+ u^2_{\mu n}J_n(\Omega)\chi_n(\Omega)\left(1-\chi_n(\Omega)\right)\\
&+ u^2_{\mu m}J_m(\Omega)\chi_m(\Omega)\left(1-\chi_m(\Omega)\right). && (65)
\end{aligned}$$

as

$$G^{(mn)}_\mu(t) = \int_0^\infty d\Omega J^{(mn)}_\mu(\Omega)\left(e^{-i\Omega t}+2\bar{n}(\Omega)\cos\Omega t\right). \quad (66)$$

Alternatively, defining a thermally weighted density

$$\tilde{J}^{(mn)}_\mu(\Omega) = J^{(mn)}_\mu(\Omega)\left(1+\bar{n}(\Omega)\right) + J^{(mn)}_\mu(-\Omega)\bar{n}(-\Omega), \quad (67)$$

this can be written compactly as

$$G^{(mn)}_\mu(t) = \int_{-\infty}^\infty d\Omega\tilde{J}^{(mn)}_\mu(\Omega)e^{-i\Omega t}. \quad (68)$$

III. NUMERICAL AND EXPERIMENTAL BENCHMARKING

To evaluate the accuracy of our approach, we next compare emission spectra calculated using Eq. (51) with both numerically exact simulation methods and experimental spectroscopic data. We begin with simulated spectra of a degenerate dimer, where the line shape expressions can be simplified analytically, in order to illustrate how the various terms in Eq. (51) determine the properties of the emission spectrum.

A. Degenerate Dimer

The degenerate dimer is characterized by the condition that $\omega_1 = \omega_2 \equiv \omega_o$, and we here consider the case of identical, uncorrelated baths, where the results of Section II E apply with $J_1(\Omega) = J_2(\Omega) \equiv J(\Omega)$. The two eigenvectors of $\tilde{H}_{\rm S}$ are then

$$|\pm\rangle = \frac{1}{\sqrt{2}}\left(|1\rangle \pm |2\rangle\right), \tag{69}$$

with optical transitions at the frequencies

$$\omega_\pm = \omega_{\rm o} \pm \tilde{V} + \frac{1}{2}\sum_k \frac{g_{nk}^2}{\Omega_k}\left(\xi_k^2 - 2\xi_k - 1\right) \tag{70}$$

$$= \omega_{\rm o} \pm \tilde{V} - \int_0^\infty d\Omega\, J(\Omega)\cdot\Omega + \frac{1}{2}\int_0^\infty d\Omega\, J(\Omega)\left(1-\chi(\Omega)\right)^2\cdot\Omega. \tag{71}$$

The first integral in Eq. (71) is the reorganization energy of the monomeric pigments, reflecting the energy released in the electronic excited state during relaxation from the vertical transition to the potential minimum. The second integral reflects a lowering of the total reorganization energy due to excitonic delocalization. Physically, this reflects the fact that delocalization of the electronic excitation across multiple pigments "dilutes" the impact of the excitation on the local bath of each individual site, since each mode "feels" only a fractional electronic excitation. With $\chi(\Omega) = 0$ (i.e., without the polaron transform), this produces an overall rescaling of $J(\Omega)$ by a factor of $\frac{1}{2}$, which is a special case of the "Inverse Participation Ratio (IPR) approximation" of Ref.[13] (See, e.g., Refs.[1,30] for alternative derivations of the same result.) The polaron transform has the effect of limiting this delocalization-induced rescaling of the reorganization energy: when $\chi(\Omega) \to 1$ (the full polaron transform), the reorganization energy becomes completely insensitive to excitonic delocalization, reflecting the fact that, in the polaron frame, each bath mode is already fully relaxed within the excited-state potential of the corresponding pigment.

Even for the degenerate dimer, the actual form of the weighting function $\chi(\Omega)$ must be determined self-consistently, but it can be shown analytically that $\chi(\Omega)$ shifts gradually from 0 in the low-frequency limit to 1 in the high-frequency limit (see Appendix C). As a result, delocalization-induced changes to the reorganization energy under the VPT will be primarily determined by the low-frequency portion of the spectral density. Thus the VPT offers a natural means of incorporating high-frequency vibrations in excitonic line shapes without the potential for (likely unrealistic) variable reorganizion-energy shifts of hundreds of wavenumbers ($\rm cm^{-1}$). (See Refs.[2,31] for relevant discussion on the role of high-frequency modes in energy transfer and optical spectra.)

To provide a concrete example of the variation of $\chi(\Omega)$ with frequency, Figure 1(a) plots the terms $\chi^2(\Omega)$ (green), $\chi(\Omega)\left(1-\chi(\Omega)\right)$ (cyan), and $\left(1-\chi(\Omega)\right)^2$ (red) computed for a degenerate dimer with $V = 170$ $\rm cm^{-1}$, a temperature of 5 K, and spectral densities $J(\Omega)$ chosen to reflect the properties of the LvWSCP complex. (See Appendix D.) Note that $\left(1-\chi(\Omega)\right)^2$ decays rapidly with frequency, dropping below 0.1 around 185 $\rm cm^{-1}$. Thus, in this and similar systems, effects like reorganization-energy rescaling that are proportional to $\left(1-\chi(\Omega)\right)^2$ will be determined almost entirely by the low-frequency phonon portion of the spectral density, with higher-frequency local vibrations playing only a minor role.

For the degenerate dimer, the emission spectrum can be expressed (see Eqs. (10) and (51)) as

$$\varepsilon(\omega) = \frac{Z_B}{Z_{\rm e}}\mu_{\rm o}^2 \sum_\pm e^{-\beta\hbar\omega_\pm}\varepsilon_\pm(\omega) \tag{72}$$

where

$$\varepsilon_\pm(\omega) = \varepsilon_{\rm loc}\left(\omega-\omega_\pm\right) \pm \varepsilon_{\rm int}\left(\omega-\omega_\pm\right), \tag{73}$$

with "local" and "interference" line shapes

$$\varepsilon_{\rm loc}(\omega) = \int_{-\infty}^\infty dt\; e^{-i\omega t} e^{G_{\rm loc}(t)-G_{\rm loc}(0)} \tag{74}$$

$$\varepsilon_{\rm int}(\omega) = e^{-\tilde{S}(T)}\cos\theta \int_{-\infty}^\infty dt\; e^{-i\omega t} e^{G_{\rm int}(t)-G_{\rm int}(0)}. \tag{75}$$

The symmetric exciton component $\varepsilon_+(\omega)$ corresponds to correlated oscillation of the local transition dipole moments, while $\varepsilon_-(\omega)$ corresponds to anticorrelated dipole motion. These two states exhibit either constructive or destructive interference depending on the angle θ between the local transition dipole moments of each monomer. The parameter

$$\tilde{S}(T) = \int_0^\infty d\Omega\; J(\Omega)\left(1+2\bar{n}(\Omega)\right)\chi^2(\Omega) \tag{76}$$

is a weighting factor analogous to a thermally (and polaron-) weighted Huang-Rhys factor. The line shape functions

$$G_x(t) = \int_{-\infty}^\infty d\Omega\, \tilde{J}_x(\Omega) e^{-i\Omega t} \tag{77}$$

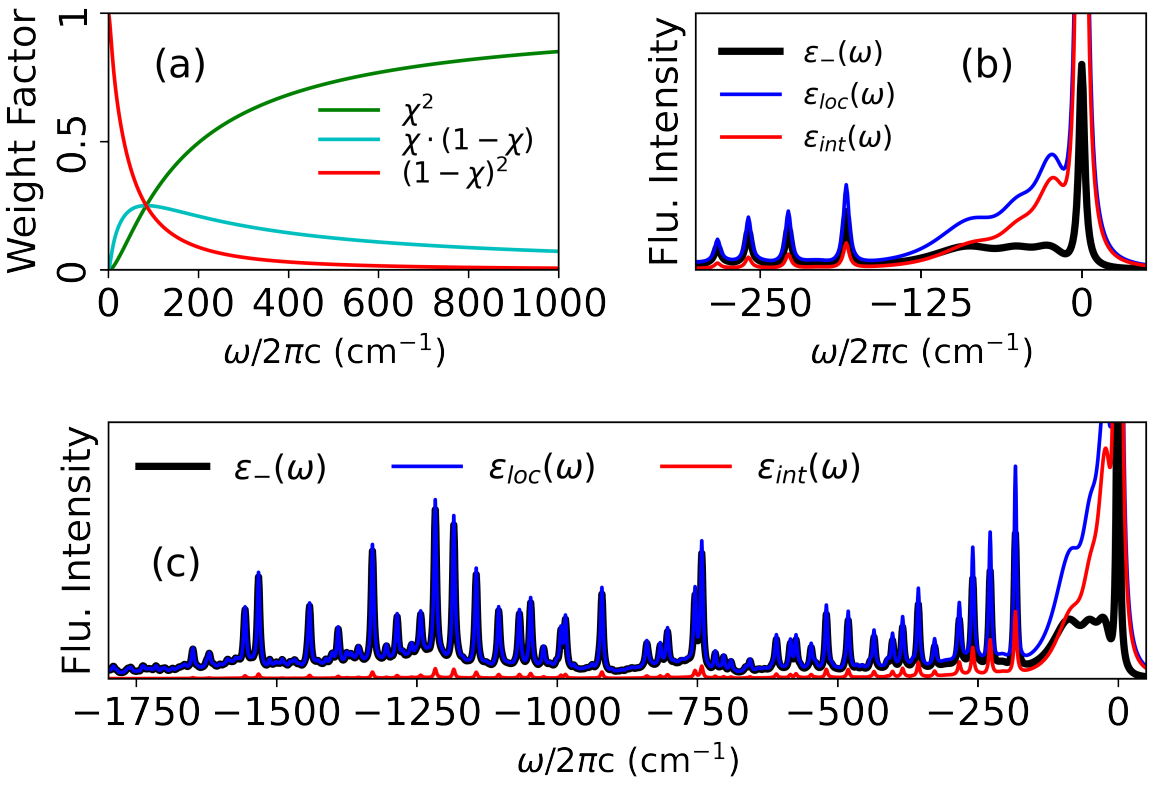

FIG. 1. Components of the degenerate dimer emission spectrum. (a): Weighting functions $\chi^2(\Omega)$ (green), $\chi(\Omega)\cdot(1-\chi(\Omega))$ (cyan), and $(1-\xi(\Omega))^2$ (red). (b) and (c): Full lower exciton band spectrum $\varepsilon_-(\omega)$ (black) and its two components $\varepsilon_{\rm loc}(\omega)$ (blue) and $\varepsilon_{\rm int}(\omega)$ (red). Frame (b) focuses on the phonon-sideband region, while Frame (c) shows the full VSB.

are determined by the effective spectral densities

$$J_{\rm loc}(\omega) = \frac{1+\chi^2(\omega)}{2} J(\omega) \tag{78}$$

$$J_{\rm int}(\omega) = \frac{1-\chi^2(\omega)}{2} J(\omega), \tag{79}$$

with

$$\tilde{J}_x(\Omega) = J_x(\Omega)\,(1+\bar{n}(\Omega)) + J_x(-\Omega)\bar{n}(-\Omega). \tag{80}$$

Frames (b) and (c) of Figure 1 illustrate the contribution of these various components to the emission spectrum of a degenerate dimer at $T = 5$ K, with an angle of $\theta = 30^{\rm o}$ between the two pigment transition dipole moments. The term $\varepsilon_{\rm loc}(\omega)$ (blue) resembles a local (incoherent) emission spectrum from each monomer, with a partially suppressed contribution from low-frequency vibrations due to the prefactor $\frac{1+\chi^2}{2}$ in $J_{\rm loc}(\omega)$: when $\chi(\Omega) \to 1$ at high frequencies, this approaches the spectrum of the isolated monomer; when $\chi(\Omega) \to 0$ at low frequencies, the vibrational density is scaled down by the IPR factor of $\frac{1}{2}$.[13]

The "interference" term $\varepsilon_{\rm int}(\omega)$, conversely, represents coherent interference between the transition dipole moments of the two pigments; the prefactor of $\frac{1-\chi^2}{2}$ that scales $J_{\rm int}(\omega)$ implies that dipole-dipole interference effects are restricted to the purely electronic transition and to the low-frequency region of the vibrational sideband. This term is proportional to both $\cos\theta$ (which determines whether the interference is destructive or constructive) and $e^{-\tilde{S}(T)}$, which suppresses interference at high temperatures. Note that this is the same factor that renormalizes the dimer coupling, i.e.,

$$\tilde{V} = e^{-\tilde{S}(T)} V, \tag{81}$$

so that in the high-temperature limit, the two monomers act as independent emitters. At intermediate temperatures, this continuous rescaling of the coupling implies also a temperature-dependent shift in the splitting between the zero-phonon lines (ZPLs) of the two polaron states, which is always equal to twice the renormalized coupling $\tilde{V}$ (see Eq. (70)).

For a dipole angle of $\theta = 30^{\rm o}$ (with $\cos\theta > 0$), the fluorescence spectrum of the lower exciton band takes the form of a scaled *difference* between $\varepsilon_{\rm loc}(\omega)$ and $\varepsilon_{\rm int}(\omega)$, so that, in the total fluorescence spectrum, the ZPL and low-frequency phonons are suppressed, while high-frequency modes exhibit nearly the same intensity as

for the uncoupled monomer transitions. In the full-polaron limit, when $\chi(\omega) \to 1$, the line shape function $G_{\rm int}(t) \to 0$, so that dipole-dipole interference affects only the purely electronic ZPL. In this regime, high-frequency vibrations act as local emitters even when the purely electronic transition remains delocalized.[7,23–25]

B. Numerical Benchmarking

To test the accuracy of this theory, we next compare calculated fluorescence spectra using the VPT method against numerically exact matrix diagonalization calculations. Briefly, these calculations involve the construction of a very large discrete representation of the complete system-bath Hamiltonian (Eq. (1)), including explicitly multiple excited states for each vibrational mode. For this comparison, we use a discrete-mode vibrational spectral density that mimics the parameters extracted from ΔFLN data on the CP29 complex, but "condensed" into a smaller number of independent modes so as to facilitate the numerically exact matrix-diagonalization methods, whose computational cost scales rapidly with the number of modes. (See Ref.[7] for a similar approach and Appendix D for further details on our simulations here.) Our intention here is not to accurately model any particular experimental system, but simply to benchmark the performance of the VPT approach against numerically exact simulations.

To this end Figure 2 compares $T = 0$ K emission spectra calculated under the two methods for a molecular dimer with relative dipole angles varying between 45° and 135°, and with varying values of the site-to-site coupling constant V and site-energy asymmetry $\omega_{12} = \omega_1 - \omega_2$. For better visibility, all spectra are convolved with a Gaussian profile with a standard deviation $\sigma = 50$ cm^{-1} and then normalized by the maximum value of the 0-0 band. In each frame, dashed curves correspond to numerical diagonalization, while solid lines represent VPT-calculated spectra.

Qualitatively, the two methods agree quite well, showing the same trends of VSB enhancement or suppression due to dipole-dipole interference. Quantitatively, the curves match almost exactly for site-to-site coupling up to ~ 100 cm^{-1}, but differences become noticeable for the $V = 400$ cm^{-1} strong coupling case. In this regime, the VSB intensity is over-estimated by the VPT, particularly when the angle between transition dipoles is set to 45°. This would appear to indicate that the VPT theory over-estimates either the excitonic *delocalization* of the 0-0 band or the dynamic *localization* of the VSB, both of which will lead to asymmetry in dipole-dipole interference between the two features. The 90° case confirms that the VPT theory indeed over-estimates vibrational localization effects, since the VSB intensity in this case is still slightly larger than in the numeric diagonalization simulation; in this case, no dipole-dipole interference effects are possible, so that the intensity of the VSB directly correlates with the *suppression* of IPR scaling by vibrational localization. (Note that the structure of the Hamiltonian and thus the polaron-transform parameters here are independent of the assumed dipole angle.) In the 135° case, the two spectra are very nearly identical; since we know already that the VSB is too localized in the VPT theory, this almost certainly indicates a cancellation of errors: a too-large enhancement of the 0-0 band due to dipole-dipole interferences is partially compensated by a too-weak suppression of the VSB due to vibrational localization. Thus, numerical benchmarking suggests that, although our VPT method captures qualitatively the correct physics across the entire sampled parameter range, for strong electronic coupling, it somewhat overestimates delocalization of the 0-0 band and underestimates delocalization in the VSB.

C. Application to WSCP Fluorescence

As an experimental test of our VPT approach, we next consider the 77 K fluorescence spectrum of the LvWSCP complex. LvWSCP binds four chlorophyll molecules in a "dimer of dimers" configuration, featuring excitonic delocalization within (but not between) each pair of dimers.[31,32] In the WT protein, two exciton bands can be distinguished in 77 K absorption measurements, corresponding roughly to the "+" and "-" dimer states of Section III A.[23] Because the pigments are bound in an H-aggregate-like geometry (with an angle of 30° between the NB→ND vectors of each pigment), the intensity of the lower exciton band is partially suppressed. In the experimental 77 K fluorescence spectra for WT WSCP (black dashed curve in Figure 3), this leads to a substantial enhancement of the vibrational sideband (VSB) between roughly 800 and 1700 cm^{-1} from the 0-0 transition, similar to (but not as dramatic as) the effect observed for the degenerate dimer in Figure 1.[23,24] In the Q57K mutant (red dashed curve in Figure 3), excitonic delocalization is disrupted, eliminating the VSB enhancement.[16,23]

We have recently shown that vibronic mixing calculations of the type described in Section III B accurately capture the VSB enhancement of the WT protein, when spectral density and static disorder parameters are fitted from the Q57K (monomer-like) fluorescence spectrum.[23] However, quantitative comparison in that case was complicated by the fact that the experimental data is measured at 77 K, while our vibronic mixing calculations are (for numerical reasons) restricted to the $T = 0$ K limit, with a discrete spectral density approximating the continuous phonon sideband observed experimentally. Since our VPT approach is not limited by these restrictions, we turn next to examining its performance in describing the same experimental data set.

The solid black curve in Figure 3, which overlaps almost exactly with the Q57K fluorescence spectrum (dashed black curve), is the spectrum of monomeric Chl *a* calculated using the single-site form of Eq. (51). (For

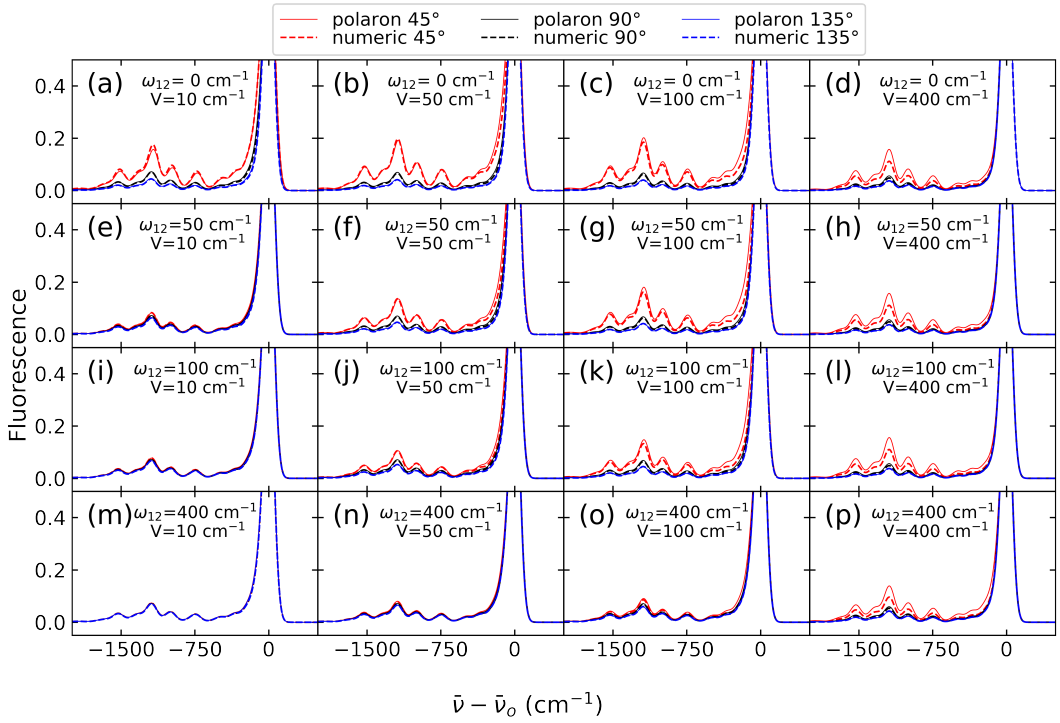

FIG. 2. Comparison of T = 0 K fluorescence spectra computed with the VPT (solid curves) and numerically exact vibronic calculations (dashed curves) for a variety of disorder ω_{12} and coupling V parameters and three values of the relative dipole angles (45° in red, 90° in black and 135° in blue). A discrete-mode spectral density of the CP29 complex is utilized. The frequency differences between monomer sites are as follows: $\omega_{12}/(2\pi c) = 0$ cm^{-1} in Frames (a) - (d); $\omega_{12}/(2\pi c) = 50$ cm^{-1} in Frames (e) - (h); $\omega_{12}/(2\pi c) = 100$ cm^{-1} in Frames (i) - (l); and $\omega_{12}/(2\pi c) = 400$ cm^{-1} in Frames (m) - (p). The inter-site coupling strength is: $V/(2\pi c) = 10$ cm^{-1} in the column headed by Frame (a); $V/(2\pi c) = 50$ cm^{-1} in the column headed by Frame (b); $V/(2\pi c) = 100$ cm^{-1} in the column headed by Frame (c); and $V/(2\pi c) = 400$ cm^{-1} in the column headed by Frame (d).

a single pigment, Eq. (51) becomes an exact solution to Eq. (7) with $\chi(\Omega) = 1$.) To account for static disorder, the calculated single-site spectrum is convolved with a Gaussian with standard deviation 100 cm^{-1}. The near-exact overlap here between theory and experiment is not a reflection on the quality of our theory, but a consequence of the fact that the Huang-Rhys (HR) factors and static disorder parameters have previously been optimized to reproduce this same experimental spectrum. (See Appendix D and Ref.[23] for details.)

The more interesting comparison is between the WT fluorescence spectrum (dashed red curve) and the VPT-calculated emission spectrum (solid red lines). In these calculations, the bare electronic coupling is set to $V = 170$ cm^{-1}, chosen so that the disorder-averaged value of the renormalized coupling $\tilde{V}$ of Eq. (23) is $\sim$85 cm^{-1}, in agreement with both previous theoretical fits to the related Cauliflower WSCP (CaWSCP) complex and structure-based TrESP-calculated couplings for LvWSCP from the PigmentHunter app.[33–36] Calculated spectra are shown here for three different assumptions on the angle between the pigment transition dipole moment. Although the crystal structure of WT LvWSCP has been solved[32] (so that the relative pigment orientation is known), there is some discrepancy in the literature over the correct orientation of the pigment transition dipoles within the molecular frame. Based on various experimental measurements, estimates range from a -7 to a +15° rotation of the dipole from the NB→ND (y) axis toward the NA→NC (x) axis,[12,37,38] corresponding (in the LvWSCP geometry) to a relative transition dipole angle of between 26° and 38°. Previous theoretical work has favored a relative dipole angle of 30°, although this conclusion is based primarily on simulation of the optical spectra of CaWSCP, a different (though related) complex extracted from cauliflower. Thus, while we expect the dipole angle for LvWSCP to be likewise close to 30°, some deviation from this value is possible.

This caveat turns out to be quite significant for our present purposes, since the intensity of the 0-0 band in the simulated fluorescence spectrum depends strongly on the assumed dipole angle. Agreement with experiment is best for $\theta \approx 45°$, although in all three cases, the intensity of the mid-frequency range near 500 - 1000 cm^{-1} is somewhat over-estimated. In light of the numerical benchmarking from Figure 2, it is likely that the favorable performance of the 45° simulation is an artifact due to too-strong suppression of the 0-0 transition relative to

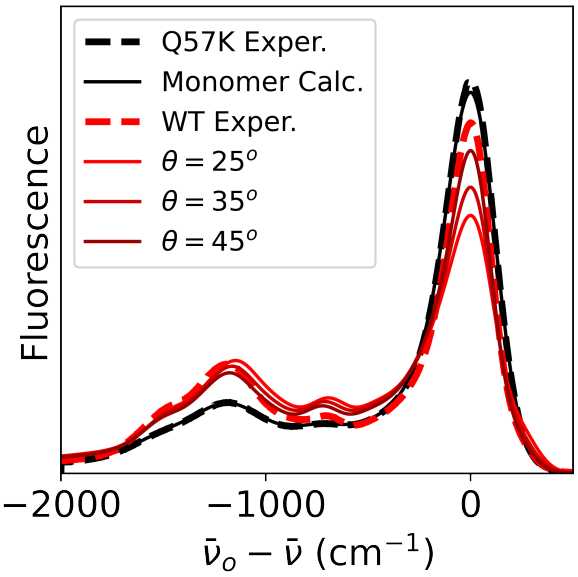

FIG. 3. Experimental (dashed curves) and calculated (solid curves) spectra for the WT and Q57K LvWSCP complexes. All spectra are normalized by area. Calculated dimer spectra are labeled by the angle θ assumed between the two pigment transition-dipole moments.

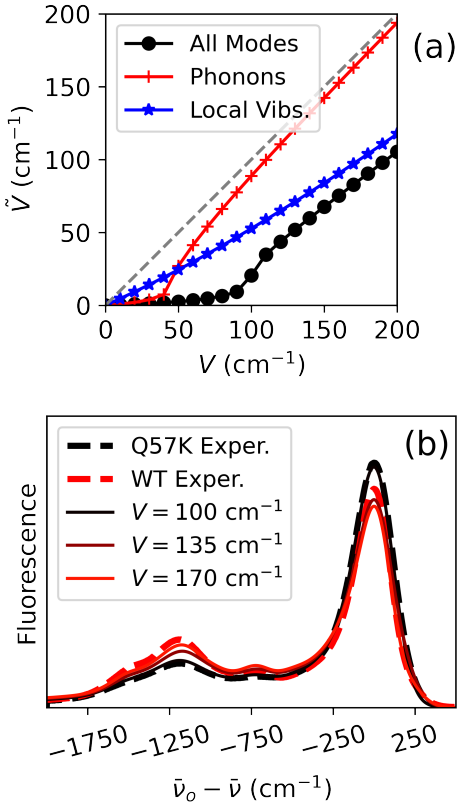

FIG. 4. (a) Rescaled coupling $\tilde{V}$ for the LvWSCP complex calculated as a function of the assumed bare electronic coupling V. Black circles denote calculations including the entire LvWSCP spectral density; blue stars represent calculations including only high-frequency discrete modes, and red "+" marks result from including only the low-frequency phonon density. (b) Experimental (dashed curves) and calculated (solid lines) 77 K emission spectra for LvWSCP parameters with $\theta = 45^o$ as a function of the bare coupling strength V. Curves are normalized by area.

the VSB. Most likely the true dipole angle is in the expected range of 30 - 35°, with the weak 0-0 transition in our VPT simulation due to the same effects described in the 45° case in Figure 2.

Thus while dipole-angle uncertainty precludes quantitative conclusions on VPT performance, this experimental comparison (especially the consistent over-estimation of mid-frequency VSB intensities) supports the conclusion from numeric benchmarking that the VPT assigns too much localized character to high-frequency vibrations. This effect is very likely related to the well-documented (and presumably unphysical) abrupt transitions sometimes observed for the variational polaron parameter ξ_k as a function of temperature.[26,28] A similar "too-abrupt" transition toward localization as a function of vibrational frequency would offer a quite plausible explanation of our results here. Nonetheless, it is encouraging to see that the VPT offers reasonable agreement with experiment without any optimization of the monomer-model parameters. We should emphasize here that the quality of the simulation will depend on additional model parameters (e.g., site energy distribution width, energy-transfer times, and relaxation across the two WSCP dimers) that we have not accounted for in these simulations. More detailed insight (including firmer constraints on the dipole angle θ) should be obtainable from future modeling studies including simultaneous simulation of a variety of types of optical spectra.[33]

IV. DISCUSSION & CONCLUSIONS

The numerical and experimental benchmarking of our VPT approach in the last section demonstrate that, at least for dimeric systems, the theory captures the correct qualitative trends in fluorescence line shape as a function of excitonic delocalization. Its chief quantitative failing appears to be an over-estimation of vibrational localization effects in the mid- to high-frequency vibrational range in systems with strong electronic coupling, accompanied by an over-estimation of the excitonic suppression of the purely electronic transition. It is encouraging, nonetheless, that the VPT approach offers at least qualitatively correct behavior across the entire range of coupling strengths and vibrational frequencies that we investigate. In this final section, we first consider what useful conclusions can be drawn from the present theory (imperfections notwithstanding) and then close with a discussion of potential avenues for further refinement.

A. Screening of Inter-pigment Interactions

One useful feature of the VPT theory is that it offers a simple and conceptually informative explanation for the effective rescaling of electronic coupling due to system-bath interactions. This phenomenon has previously been observed using numerical diagonalization methods (see Figure 4 of Ref.[7]), where it was interpreted in light of the decohering effect of local vibrations on the lowest-energy eigenstate at zero Kelvin. Our present results allow for a more thorough examination of this effect through the explicit renormalization of site-to-site interactions in the variational polaron frame. Recall from Eq. (23) that, in the polaron frame, the electronic coupling V_{mn} between system sites is damped by a thermally averaged factor $\left\langle \hat{\Delta}_{mn} \right\rangle_{\mathrm{B}}$ that reflects the reorganization of the bath when the electronic excitation is transferred from site m to n. Physically, this corresponds to a partial offset of the the electronic interaction energy by bath reorganization, similar to the way that environmental polarization partially offsets electrostatic interactions in dielectric media. Indeed, at an atomistic level, electrostatic screening is one very likely origin of such effects, since polarization of the environment is expected to contribute to electron-phonon coupling.

As in dielectric media, however, electronic screening depends on the ability of the bath to reorganize on a faster time scale than the system dynamics. If the electronic excitation oscillates between two sites on a time scale much faster than the corresponding bath modes can respond, there will be no time for the bath to reorganize and, thus, no screening of the electronic interaction. In the VPT theory, this is reflected by the frequency-dependence of the variational parameter ξ_k for each mode or its continuous analog $\chi(\Omega)$. The fact that $\chi(\Omega) \to 0$ when $\Omega \to 0$ means that very low-frequency modes do not contribute to the rescaling parameter $\left\langle \hat{\Delta}_{mn} \right\rangle_{\mathrm{B}}$, while the fact that $\chi(\Omega) \to 1$ when $\Omega \to \infty$ means that high-frequency modes will always contribute to the rescaling. Which modes qualify as "low-frequency" and "high-frequency" depends on the system characteristics through the variational optimization of $\chi(\Omega)$.

To illustrate this effect more precisely, Figure 4(a) plots the rescaled coupling $\tilde{V}$ as a function of the bare electronic coupling V for a molecular dimer calculated with three different sets of system-bath spectral densities. Black data points correspond to the full spectral density used for LvWSCP calculations in Figure 3; blue stars correspond to only the high-frequency "local vibration" component of this density; and red '+' marks correspond to only the continuous low-frequency portion of the spectral density.

For the high-frequency "local vibrations" density, the effect of the bath is to produce a simple, nearly linear, rescaling of the bare electronic coupling, with a slope of roughly $\frac{1}{2}$; this reflects the fact that across the entire range from $V = 0$ cm^{-1} to $V = 200$ cm^{-1}, most high-frequency vibrations are able to reorganize on a time scale faster than the frequency of electronic energy transfer between the two sites. (Note that the slope of $\sim \frac{1}{2}$ here is a consequence of the specific vibrational spectral density, with no direct relation to the number of sites or IPR.) By contrast, when only phonons are included, electronic coupling is damped heavily when $V \lesssim 50$ cm^{-1}, but damping almost completely disappears by $V \approx 100$ cm^{-1}, reflecting the fact that the phonon density peaks around 28 cm^{-1} and tends quickly toward zero past 100 cm^{-1} (see Figure 1(b)).

Rescaling under the full density (black data points) combines features of both individual densities, though not in a simple additive or multiplicative manner: here damping begins to weaken substantially only when $V \approx 100$ cm^{-1}, tending ultimately toward the local vibration damping line. This nonlinearity of the effective damping strength reflects the fact that, in the VPT, the screening of electronic interactions by one set of bath modes tends to enhance the renormalization effect of other bath modes, since weakened electronic coupling produces further bath reorganization, which, in turn, further weakens the electronic coupling.

Regardless of quantitative accuracy, the trends exhibited in Figure 4 suggest a simple explanation for at least one open question regarding the LvWSCP Q57K mutant: How is it that a single point mutation is sufficient to completely eliminate electronic coupling, at least so far as can be discerned from circular dichroism[16] and fluorescence spectra?[23] This experimental result indeed seems somewhat surprising, since (despite weakened stability) the complex appears in native gel electrophoresis and infrared spectroscopy measurements to remain largely folded in the same tetrameric structure as the WT.[16] From a structural perspective, it seems puzzling that the Q57K mutant complex is able to accommodate the same four pigments into a folded tetrameric structure *without* allowing them to interact electronically.

The highly nonlinear relationship between V and $\tilde{V}$ in Figure 4(a) offers a simple resolution to this puzzle: very likely, the pigments *do* interact electronically in the Q57K complex, with only a modest decrease in the bare electronic coupling energy. Because the effective coupling strength $\tilde{V}$ drops precipitously around 100 cm^{-1}, the site-to-site coupling strength need only decrease to around this value for the effects of excitonic delocalization to be almost completely eliminated. Figure 4(b) illustrates this effect by plotting calculated fluorescence spectra for a coupled dimer with the full LvWSCP spectral density, a rotation angle of $\theta = 45^{\circ}$ between the transition dipole moments, and bare electronic coupling values of 100, 135, and 170 cm^{-1}. For ease of comparison (not necessarily for physical accuracy), the dipole angle of 45° is set here so that the $V = 170$ cm^{-1} spectrum matches very closely with the WT experimental data. As expected, the $V = 130$ cm^{-1} spectrum exhibits a slight drop in VSB intensity, while the $V = 100$ cm^{-1} spectrum

is already almost identical to that of the Q57K mutant, with a disorder-averged $\tilde{V}$ value of only 22 cm^{-1}.

Thus we suggest that the most likely explanation for the behavior of the Q57K mutant is that mutation-induced distortion of the protein structure produces a modest drop in the bare electronic coupling, on the order of 70 cm^{-1} (a 41% decrease if the WT coupling is taken to be $\sim$ 170 cm^{-1}). Such a decrease is not difficult to rationalize even within a stable protein structure due, for example, to small shifts in the inter-pigment spacing or transition dipole orientation, particularly since the Q57K mutation alters a hydrogen-bonding network that directly interacts with the Chl *a* ring-V keto group. Even such a modest drop, however, brings the electronic coupling frequency into the range that is effectively damped by the low-frequency phonon sideband, so that the *effective* electronic coupling drops much more dramatically, eliminating the observed delocalization effects in fluorescence and CD spectra.

B. Phonon Sideband Shapes

A second advantage of the VPT theory compared to most numerically exact methods is that it is agnostic as to the functional form of the spectral density. In contrast, numerical diagonalization methods rely on a discrete representation of the bath density, with computational expense scaling in a highly nonlinear fashion with the number of modes.[7,23,24] Conversely, methods based on the hierarchical equations of motion (HEOM) work optimally for high temperatures and smooth Drude-Lorenz spectral densities, although (at substantial numerical cost) other spectral densities can be accommodated.[39–42] Path integral methods provide one of very few options for numerically exact spectroscopy simulations with arbitrary spectral densities, and in future work it should be quite informative to directly benchmark our VPT approach against such simulations.[43]

For the present, we wish to take advantage of the VPT theory's flexibility to address only one additional question regarding the interpretation of LvWSCP spectroscopic data: What is the expected impact of excitonic delocalization on the experimentally measured shape and overall coupling strength of the low-frequency phonon sideband (PSB)? A series of careful ΔFLN measurements for the related Cauliflower WSCP (CaWSCP) revealed a broad PSB with a peak frequency of 28 cm^{-1}, an apparent overall HR factor of S = 0.81, and an unusual multi-mode structure with peaks at roughly 28, 54, and 90 cm^{-1}.[44] For illustration, the black curve in Figure 5 represents the fluorescence line shape for a monomeric pigment with this spectral density, using the log-normal functional form of Ref.[45] and with the time-domain line shape function damped by an exponential decay over 10 ps to provide a finite line width. (A complete set of high-frequency vibrations is also included, as in Figure 3, but is not visible due to the frequency limits.)

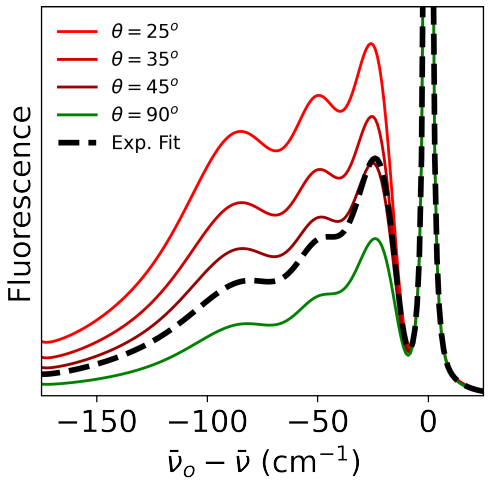

FIG. 5. Comparison of calculated, disorder-averaged single-site fluorescence spectra for the WSCP dimer (solid lines) with a monomer-like spectrum (dashed line) parameterized to mimic the ΔFLN line shape of the CaWSCP complex.

Although CaWSCP and LvWSCP differ in structural details, the overall pigment-binding geometry is similar, leading to the same partial suppression of the lower-exciton band in absorption and relative enhancement of the VSB. Since the PSB extends across more than 100 cm^{-1} in frequency, the impact on PSB line shape of the competing effects of excitonic delocalization and vibrational localization is difficult to predict *a priori*. For example, is the measured S factor for the WT CaWSCP protein likely to be inflated relative to the monomeric pigment due to the excitonic suppression of ZPL intensity? Or is the experimental S value artificially suppressed due to excitonic IPR rescaling?

Adolphs et al. examined this question previously using a non-Markovian line-shape theory that included IPR suppression of the PSB but not the frequency dependence of vibrational localization offered by the VPT treatment.[46] Two important conclusions of that study were that (1) the true phonon HR factors for each local site are somewhat higher (around $S = 1.15$) than the effective HR factors (around $S = 0.8$) measured directly in experiment; and (2) that the local HR factors vary significantly as a function of frequency across the inhomogeneous pigment ensemble. The immediate question for our discussion now becomes: to what extent will these conclusions be altered by frequency-dependent vibrational localization and the associated relative enhancement of higher-frequency modes)?

To address this question, Figure 5 presents calculated spectra for a model dimer with the same parameters as in Figure 3 but with a different treatment of site-to-site disorder. Namely, the spectra in Figure 5 are averaged over 100 different (Gaussian-weighted) values of the site-energy difference $\omega_{12} = \omega_1 - \omega_2$, but with all

spectra shifted to the same ZPL frequency *before* averaging. Although this procedure is by no means a quantitative replica of a ΔFLN measurement (in which the probability of excitation at a fixed excitation wavelength depends directly on the asymmetry ω_{12}), it provides at least a qualitative description of the disorder-averaged single-site fluorescence spectrum that is measured in a ΔFLN experiment.[47,48] All spectra are normalized by the maximum value of the ZPL.

For a monomeric pigment (with suitably weak electron-phonon coupling), the intensity of the PSB in such a spectrum is directly proportional to the overall phonon HR factor S.[49] Thus if the calculated curves in Figure 5 were interpreted within the standard description for a monomeric pigment, one would incorrectly conclude that the overall S factor is much larger in the $\theta = 25^o$ case than the true value. In reality, this "enhancement" of the PSB is instead due to the strong suppression of the ZPL by coherent dipole-diple interference. This relative enhancement is larger for the high-frequency portion of the PSB, which is why the line shape appears distorted relative to the monomer spectrum. These effects are less pronounced for the $\theta = 35^o$ case, and for $\theta = 45^o$ the overall area of the PSB becomes nearly the same for monomer and dimer spectra, as the weakened suppression of the ZPL begins to be just balanced by the IPR scaling that tends to lower the PSB intensity. For comparison, the green curve in Figure 3 shows the dimer spectrum calculated for orthogonal dipoles, i.e., with $\theta = 90^o$, where dipole-dipole interference effects are absent and IPR scaling suppresses the PSB below the experimental curve. This $\theta = 90^o$ curve is the most directly comparable (though not identical) to the calculations of Ref.[46] since that study included IPR scaling for the entire PSB but with no mechanism for relative enhancement of higher-frequency vibrations.

What does this comparison imply with regard to real CaWSCP ΔFLN data? Although a complete answer must wait for more careful simultaneous fitting studies (as reported by Adolphs et al.[46]), two qualitative conclusions can be drawn. First, the experimentally extracted PSB density almost certainly over-emphasizes the higher frequency PSB components relative to the 28 cm^{-1} band. Due to the preferential suppression of low-frequency modes in the excitonic system, the true intensity of the 28 cm^{-1} mode in the true "monomer" spectral density will need to be substantially higher than what is directly measured experimentally to give the correct peak-height ratios in the dimer. Indeed, it is tempting to speculate that the 54 cm^{-1} component observed in experiment might be a two-phonon overtone of the 28 cm^{-1} component, artificially enhanced due to its relatively higher frequency, though more careful fitting than we provide here would be necessary to validate this hypothesis.

Second, the overall value of $S = 0.81$ extracted from the experimental spectrum is likely an over-estimate, due to the suppression of the ZPL in the coupled dimer by dipole-dipole interference. The magnitude of this effect depends strongly on the assumed value of θ, but (since the true value is probably in the range of 30^o to 35^o), the true "monomer" HR value is likely to be substantially lower than the original estimate of $S = 0.81$. This second conclusion is in contrast with the conclusions of both Adolphs et al.[46] and Ref.[7], which anticipated the *under*-estimation of PSB HR factors from monomer-like fits to experimental ΔFLN measurements. As pointed out in Ref.[24], this argument is correct only for the special case of orthogonal dipole moments. When dipole-dipole interference effects are significant, either overestimation or underestimation is possible, depending on the degree of excitonic suppression or enhancement of the ZPL.

Beyond this qualitative assesment, quantitative evaluation of the true HR factor in WSCP must await more detailed fitting studies and, ideally, validation by comparison to new experimental ΔFLN measurements on WSCP mutants that lack electronic delocalization. By comparing spectra from the delocalized WT protein with spectra from the "localized" Q57K mutant,[23] it should be possible to disentangle with some precision which line shape features are associated with the local HR factors of the pigment-binding site and which factors are due to excitonic effects.

Our present calculations are likewise too simplistic to offer detailed insight into the frequency-dependence of the S factor,[44] although it is likely that accurately accounting for vibrational localization will at least partially offset the trend reported by Adolphs et al.[46] In the latter study, the experimentally observed *decrease* of HR factor with excitation wavelength[44] was found to run counter to the trend that the delocalization also decreases with excitation wavelength – which, according to IPR scaling, should tend rather to *increase* the effective S factor at long wavelengths). Hence, it was concluded that the true local HR factor varies with wavelength even more strongly than the experimentally observed effective HR factor. Although we can draw no quantitative conclusions from the simple model calculations of Fig. 5, the fact that our VPT theory predicts an overall *increase* of PSB intensity due to excitonic delocalization (in constrast to the decrease predicted by IPR scaling) suggests a different interpretation of the experimental results: namely, that the loss of excitonic delocalization with increasing wavelength could result in an apparent decrease in measured PSB intensity, even if the true local HR factor is identical for all sites. Whether this mechanism can quantitatively account for the measured experimental trend remains an open question that must await more detailed experimental and computational studies.

C. Future Prospects

While the VPT approach developed here offers important insight into the interplay between excitonic delocalization and vibrational localization, there are several

important areas where the theory could be improved in future work. Perhaps the most important limitation of the theory presented here is that we consider only pure-dephasing processes, i.e., the present approach fails to account for relaxation between polaron states. While this has little impact on the 0 K - 77 K fluorescence spectra we consider here (where virtually all signal is from the long-lived lowest exciton state), accurate inclusion of relaxation processes will be critical for treating not only time-domain and room-temperature signals but also frequency-domain measurements like absorption, circular dichroism, and hole burning, where energy-transfer broadening in the upper exciton bands strongly impacts the calculated line shape.[33,50] Fortunately, a rich literature of VPT-based methods already exists for treating such relaxation processes,[14] with a recent report by Jang most closely mirroring the approach we follow here.[15] Merging these two approaches will be technical but should, in principle, not be difficult, and it will be critical to accurately describe a wide range of optical phenomena.

Another potential opportunity for improvement follows from the development in recent years of multiple numerically exact approaches to treating vibrational-exciton dynamics, including various HEOM approaches,[39–42] path-integral methods,[43] and explicit numerical diagonalization schemes.[7,24] The ability to directly benchmark VPT calculations against such exact methods offers an intriguing opportunity to learn which features of the method fail and under what circumstances. For example, in our benchmarking against numerical diagonalization (see Figure 2), we see the most significant discrepancies in the case of the degenerate dimer, with small coupling values. Specifically, the calculated spectra indicate that the VPT method in these circumstances *under*-estimates suppression of the 0-0 band, suggesting that the variational optimization procedure used to calculate $\chi(\Omega)$ assigns too much polaron character to the system. With a sufficient body of numerical benchmarking data, it should be possible to establish under what circumstances such discrepancies occur, hopefully leading the way toward systematic corrections (or even numerically trained algorithms) that provide more realistic predictions across a broad range of physical parameters. In this regard, it should be emphasized that there is no *a priori* guarantee that the free-energy-maximization approach[14,29] typically used to optimize the transform weighting functions $\chi_n(\Omega)$ is the optimal solution for all types of measurements. Indeed, the traditional optimization is known to exhibit abrupt and physically questionable jumps in value as a function of temperature,[26,28] supporting the notion that alternative choices – grounded in new physical arguments, numeric benchmarking, or some combination of the two – could improve performance.

Finally, even without reference to outside methods, our VPT approach could obviously be improved by a higher-level treatment of system-bath interactions in the polaron frame. In our present approach, we drop entirely the transformed system-bath interaction operator $\tilde{B}^{(2)}_{\mu\nu}$ in the polaron frame, and retain only the diagonal components of the untransformed interaction operator $\tilde{B}^{(2)}_{\mu\nu}$ (see Eq. (30)). As examined in detail by Jang, these terms are essential drivers of energy-transfer dynamics in VPT theory,[15] and (even beyond energy-transfer broadening) may offer opportunities for systematically improving calculated line shape functions.

To summarize, the introduced VPT approach captures the essential physics of vibrational-electronic interactions in various regimes of coupling strength, disorder, and spectral densities without the heavy computational burden of exact numerical or HEOM models. Future developments promise to make the VPT approach an essential tool for understanding energy transfer and dynamics in open quantum systems.

ACKNOWLEDGMENTS

This research was supported by the U.S. Department of Energy, Office of Science, Basic Energy Sciences, under award DE-SC0022884 and by the National Science Foundation under Grant CHE-2236625. L.V.S. acknowledges the support of the National Science Foundation (grant CHE-2102639) and the Department of Energy, Office of Basic Energy Sciences (Grant DE-SC0018239). This research was partly supported through computational resources provided by Information Technology at Purdue, West Lafayette, Indiana. .

V. DATA AVAILABILITY STATEMENT

The data that support the findings of this study are available from the corresponding author upon reasonable request.

Appendix A: Rescaled Coupling Coefficients

In the Polaron frame, the site-to-site coupling constants are rescaled by the coefficients

$$\left\langle \hat{\Delta}_{mn} \right\rangle_{\mathrm{B}} = \left\langle e^{\sum_k (z_{mk}-z_{nk})\left(\hat{A}_k^\dagger - \hat{A}_k\right)} \right\rangle_{\mathrm{B}} \tag{A1}$$

$$= Z_{\mathrm{B}}^{-1} \mathrm{Tr}\left\{ e^{\sum_k (z_{mk}-z_{nk})\left(\hat{A}_k^\dagger - \hat{A}_k\right)} e^{-\beta \hat{H}_{\mathrm{B}}} \right\}_{\mathrm{B}}. \tag{A2}$$

Because the bath modes are uncoupled, the trace can be carried out for each mode independently. For each mode, the trace has the form (dropping the subscript k

for brevity):

$$\begin{aligned}
&\mathrm{Tr_B}\left\{e^{z^*\hat{A}^\dagger - z\hat{A}} e^{-\beta\hbar\Omega\hat{A}^\dagger\hat{A}}\right\} \\
&= e^{-\frac{|z|^2}{2}} \mathrm{Tr_B}\left\{e^{z^*\hat{A}^\dagger} e^{-z\hat{A}} e^{-\beta\hbar\Omega\hat{A}^\dagger\hat{A}}\right\} && \text{(A3)} \\
&= e^{-\frac{|z|^2}{2}} \sum_{\nu=0}^{\infty} e^{-\nu\beta\hbar\Omega} \left\langle \nu \left| e^{z^*\hat{A}^\dagger} e^{-z\hat{A}} \right| \nu \right\rangle && \text{(A4)} \\
&= e^{-\frac{|z|^2}{2}} \sum_{\nu=0}^{\infty} e^{-\nu\beta\hbar\Omega} \sum_{N=0}^{\nu} \frac{(-1)^\nu |z|^{2N}}{(N!)^2} \\
&\quad \times \left\langle \nu \left| \left(\hat{A}^\dagger\right)^N \hat{A}^N \right| \nu \right\rangle && \text{(A5)} \\
&= e^{-\frac{|z|^2}{2}} \sum_{\nu=0}^{\infty} \left(e^{-\beta\hbar\Omega}\right)^\nu \sum_{N=0}^{\nu} \frac{(-1)^\nu |z|^{2N}}{(N!)^2} \frac{\nu!}{(\nu-N)!} && \text{(A6)} \\
&= e^{-\frac{|z|^2}{2}} \sum_{\nu=0}^{\infty} \left(e^{-\beta\hbar\Omega}\right)^\nu L_\nu\left(|z|^2\right), && \text{(A7)}
\end{aligned}$$

where $L_\nu(x)$ is the ν^{th} Laguerre polynomial. To obtain this result, we applied in Eq. (A3) the identity

$$e^{\hat{X}+\hat{Y}} = e^{\hat{X}} e^{\hat{Y}} e^{-\frac{1}{2}[\hat{X},\hat{Y}]}, \tag{A8}$$

which holds when both $\hat{X}$ and $\hat{Y}$ commute with $\left[\hat{X},\hat{Y}\right]$. In Eq. (A6), we expanded both exponentials in the Taylor series $e^x = \sum_N \frac{x^N}{N!}$ and kept only the diagonal terms with $N \le \nu$ since all other terms are identically zero.

The Laguerre polynomials satisfy the generating function relation[27]

$$\sum_{\nu=0}^{\infty} \lambda^\nu L_\nu(x) = \frac{1}{1-\lambda} e^{-\frac{x\lambda}{1-\lambda}}. \tag{A9}$$

With $\lambda = e^{-\beta\hbar\Omega}$, this gives

$$\mathrm{Tr_B}\left\{e^{z^*\hat{A}^\dagger - z\hat{A}} e^{-\beta\hbar\Omega\hat{A}^\dagger\hat{A}}\right\} = \frac{e^{-\frac{|z|^2}{2}(1+2\bar{n}(\Omega))}}{1-e^{-\beta\hbar\Omega}}. \tag{A10}$$

Normalizing by the partition function

$$Z_{\mathrm{B}} = \sum_{\nu=0}^{\infty} \left(e^{-\beta\hbar\Omega}\right)^\nu = \frac{1}{1-e^{-\beta\hbar\Omega}} \tag{A11}$$

gives finally

$$\left\langle e^{z^*\hat{A}^\dagger - z\hat{A}} \right\rangle_{\mathrm{B}} = e^{-\frac{|z|^2}{2}(1+2\bar{n}(\Omega))}. \tag{A12}$$

Applying this result to each bath mode in Eq. (24) gives Eq. (25).

Appendix B: Emission Line Shape Function

The bath average in Eq. (47) can be factorized into separate averages over each vibrational mode k, where the quantity to be averaged has the form

$$e^{i\Omega t\hat{A}^\dagger\hat{A}} e^{x\left(\hat{A}^\dagger - \hat{A}\right)} e^{-i\Omega t\hat{A}^\dagger\hat{A}} e^{y\left(\hat{A}^\dagger - \hat{A}\right)}.$$

(Here we omit the mode index k for brevity.) The first term can be written

$$e^{i\Omega t\hat{A}^\dagger\hat{A}} e^{x\left(\hat{A}^\dagger - \hat{A}\right)} e^{-i\Omega t\hat{A}^\dagger\hat{A}} = e^{x\left(e^{i\Omega t}\hat{A}^\dagger - e^{-i\Omega t}\hat{A}\right)}. \tag{B1}$$

This follows from the identities

$$e^{i\Omega t\hat{A}^\dagger\hat{A}} \hat{A}^\dagger e^{-i\Omega t\hat{A}^\dagger\hat{A}} = e^{i\Omega t}\hat{A}^\dagger \tag{B2}$$

$$e^{i\Omega t\hat{A}^\dagger\hat{A}} \hat{A} e^{-i\Omega t\hat{A}^\dagger\hat{A}} = e^{-i\Omega t}\hat{A} \tag{B3}$$

and

$$e^{i\hat{X}} e^{\hat{Y}} e^{-i\hat{X}} = e^{e^{i\hat{X}}\hat{Y}e^{-i\hat{X}}}. \tag{B4}$$

Eq. (B2) can be obtained by noting that for any vibrational eigenstate $|\nu\rangle_{\mathrm{vib}}$ with quantum number ν,

$$\begin{aligned}
e^{i\Omega t\hat{A}^\dagger\hat{A}} \hat{A}^\dagger e^{-i\Omega t\hat{A}^\dagger\hat{A}} |\nu\rangle_{\mathrm{vib}} &= e^{-i\nu\Omega t} e^{i\Omega t\hat{A}^\dagger\hat{A}} \hat{A}^\dagger |\nu\rangle_{\mathrm{vib}} \\
&= \sqrt{\nu} e^{-i\nu\Omega t} e^{i\Omega t\hat{A}^\dagger\hat{A}} |\nu+1\rangle_{\mathrm{vib}} && \text{(B5)} \\
&= \sqrt{\nu} e^{-i\nu\Omega t} e^{i(\nu+1)\Omega t} |\nu+1\rangle_{\mathrm{vib}} && \text{(B6)} \\
&= e^{i\Omega t}\hat{A}^\dagger |\nu\rangle_{\mathrm{vib}}. && \text{(B7)}
\end{aligned}$$

Eq. (B3) follows similarly. Eq. (B4) is obtained by expanding

$$e^{i\hat{X}} e^{\hat{Y}} e^{-i\hat{X}} = \sum_{N=0}^{\infty} e^{i\hat{X}} \frac{\hat{Y}^N}{N!} e^{-i\hat{X}} \tag{B8}$$

and inserting the identity $e^{i\hat{X}} e^{-i\hat{X}} = 1$ between each pair of $\hat{Y}$ factors.

From Eq. (B1), we obtain

$$\begin{aligned}
&e^{i\Omega t\hat{A}^\dagger\hat{A}} e^{x\left(\hat{A}^\dagger - \hat{A}\right)} e^{-i\Omega t\hat{A}^\dagger\hat{A}} e^{y\left(\hat{A}^\dagger - \hat{A}\right)} \\
&= e^{x\left(e^{i\Omega t}\hat{A}^\dagger - e^{-i\Omega t}\hat{A}\right)} e^{y\left(\hat{A}^\dagger - \hat{A}\right)} && \text{(B9)} \\
&= e^{\frac{xy}{2} 2i\sin\Omega t} e^{x\left(e^{i\Omega t}\hat{A}^\dagger - e^{-i\Omega t}\hat{A}\right) + y\left(\hat{A}^\dagger - \hat{A}\right)} && \text{(B10)} \\
&= e^{\frac{xy}{2} 2i\sin\Omega t} e^{\left(xe^{i\Omega t} + y\right)\hat{A}^\dagger - \left(xe^{-i\Omega t} + y\right)\hat{A}} && \text{(B11)}
\end{aligned}$$

by noting that

$$\left[\left(e^{i\Omega t}\hat{A}^\dagger - e^{-i\Omega t}\hat{A}\right), \left(\hat{A}^\dagger - \hat{A}\right)\right] = 2i\sin\Omega t \tag{B12}$$

and applying Eq. (A3), this time to combine two exponentials into one. Using Eq. (A12), the bath average can now be evaluated directly to produce

$$\begin{aligned}
&\left\langle e^{i\Omega t\hat{A}^\dagger\hat{A}} e^{x\left(\hat{A}^\dagger - \hat{A}\right)} e^{-i\Omega t\hat{A}^\dagger\hat{A}} e^{y\left(\hat{A}^\dagger - \hat{A}\right)} \right\rangle \\
&= e^{-xy\left(e^{-i\Omega t} + 2\bar{n}(\Omega)\cos\Omega t\right)} e^{-\frac{x^2+y^2}{2}(1+2\bar{n}(\Omega))}. && \text{(B13)}
\end{aligned}$$

Substitution into Eq. (47) gives

$$\begin{aligned}
&\left\langle e^{\frac{i}{\hbar}\hat{H}_{\mathrm{B}}t}\tilde{D}^{\dagger}_{\mu\mu}\hat{D}_{\mu\kappa}e^{-\frac{i}{\hbar}\tilde{H}_{\mathrm{B}}t}\hat{D}^{\dagger}_{\lambda\mu}\tilde{D}_{\mu\mu}e^{-\beta\tilde{H}_{\mathrm{B}}}\right\rangle_{\mathrm{B}} \\
&= \sum_{n,m} u_{\mu n}u_{\kappa n}u_{\lambda m}u_{\mu m} \\
&\quad \times e^{\sum_k\left[z_{mk}+\frac{g_{\mu k}}{\Omega_k}\right]\left[z_{nk}+\frac{g_{\mu k}}{\Omega_k}\right]\left(e^{-i\Omega t}+2\bar{n}(\Omega)\cos\Omega t\right)} \\
&\quad \times e^{-\sum_k\frac{\left[z_{mk}+\frac{g_{\mu k}}{\Omega_k}\right]^2+\left[z_{nk}+\frac{g_{\mu k}}{\Omega_k}\right]^2}{2}(1+2\bar{n}(\Omega))} \qquad \text{(B14)}
\end{aligned}$$

Since

$$\frac{z_{nk}^2+z_{mk}^2}{2} = z_{nk}z_{mk}+\frac{1}{2}\left(z_{nk}-z_{mk}\right)^2, \qquad \text{(B15)}$$

this can be written

$$\begin{aligned}
&\left\langle e^{\frac{i}{\hbar}\hat{H}_{\mathrm{B}}t}\tilde{D}^{\dagger}_{\mu\mu}\hat{D}_{\mu\kappa}e^{-\frac{i}{\hbar}\tilde{H}_{\mathrm{B}}t}\hat{D}^{\dagger}_{\lambda\mu}\tilde{D}_{\mu\mu}e^{-\beta\tilde{H}_{\mathrm{B}}}\right\rangle_{\mathrm{B}} \\
&= \sum_{n,m} u_{\mu n}u_{\kappa n}u_{\lambda m}u_{\mu m} \\
&\quad \times e^{\sum_k\left[z_{mk}z_{nk}+(z_{mk}+z_{nk})\frac{g_{\mu k}}{\Omega_k}+\frac{g_{\mu k}^2}{\Omega_k^2}\right]\left(e^{-i\Omega_k t}+2\bar{n}(\Omega_k)\cos\Omega_k t\right)} \\
&\quad \times e^{-\sum_k\left(\frac{z_{mk}^2+z_{nk}^2}{2}+(z_{mk}+z_{nk})\frac{g_{\mu k}}{\Omega_k}+\frac{g_{\mu k}^2}{\Omega_k^2}\right)(1+2\bar{n}(\Omega_k))} \qquad \text{(B16)} \\
&= \sum_{n,m} u_{\mu n}u_{\kappa n}u_{\lambda m}u_{\mu m}e^{-\sum_k\frac{(z_{nk}-z_{mk})^2}{2}(1+2\bar{n}(\Omega_k))} \\
&\quad \times e^{G_{\mu}^{(mn)}(t)-G_{\mu}^{(mn)}(0)}. \qquad \text{(B17)}
\end{aligned}$$

with $G_{\mu}^{(mn)}(t)$ given by Eq. (49).

Appendix C: Variational Optimization

The optimal values of the coefficients ξ_k are chosen by adjusting their values to minimize the free energy[14,26,28,29]

$$A_{\mathrm{B}} = -\frac{1}{\beta}\ln \mathrm{Tr}_{\mathrm{S,B}}\left\{e^{-\beta\left(\tilde{H}_{\mathrm{S}}+\tilde{H}_{\mathrm{B}}\right)}\right\}. \qquad \text{(C1)}$$

Minimizing with respect to the ξ_k coefficients leads to the condition

$$\frac{\partial A_{\mathrm{B}}}{\partial \xi_k} = \frac{\mathrm{Tr}_{\mathrm{S,B}}\left\{e^{-\beta\tilde{H}_{\mathrm{B}}}e^{-\beta\tilde{H}_{\mathrm{S}}}\frac{\partial\tilde{H}_{\mathrm{S}}}{\partial\xi_k}\right\}}{\mathrm{Tr}_{\mathrm{S,B}}\left\{e^{-\beta\left(\tilde{H}_{\mathrm{S}}+\tilde{H}_{\mathrm{B}}\right)}\right\}} = 0, \qquad \text{(C2)}$$

which is equivalent to simply

$$\mathrm{Tr}_{\mathrm{S}}\left\{e^{-\beta\tilde{H}_{\mathrm{S}}}\frac{\partial\tilde{H}_{\mathrm{S}}}{\partial\xi_k}\right\} = 0. \qquad \text{(C3)}$$

Noting that

$$\frac{\partial\lambda_n}{\partial\xi_k} = 2\left(1-\xi_k\right)\frac{g_{nk}^2}{\Omega_k} \qquad \text{(C4)}$$

and

$$\frac{\partial}{\partial\xi_k}\left\langle\hat{\Delta}_{mn}\right\rangle_{\mathrm{B}} = \frac{\partial}{\partial\xi_k}e^{-\sum_k\frac{\xi_k^2}{2\Omega_k^2}(g_{mk}-g_{nk})^2(1+2\bar{n}(\Omega_k))} \qquad \text{(C5)}$$

$$= -\frac{\xi_k}{\Omega_k^2}\left(g_{mk}-g_{nk}\right)^2\left(1+2\bar{n}(\Omega_k)\right)\left\langle\hat{\Delta}_{mn}\right\rangle_{\mathrm{B}} \qquad \text{(C6)}$$

the optimization condition becomes

$$\xi_k = \left[1-\frac{\sum_\kappa e^{-\beta\hbar\tilde{\omega}_\kappa}\sum_{m,n}u_{\kappa m}u_{\kappa n}\frac{\tilde{V}_{mn}}{\Omega_k}\frac{\left(g_{mk}-g_{nk}\right)^2}{2\Omega_k^2}\left(1+2\bar{n}(\Omega_k)\right)}{\sum_\kappa e^{-\beta\hbar\tilde{\omega}_\kappa}\sum_n u_{\kappa n}^2\frac{g_{nk}^2}{\Omega_k^2}}\right]^{-1}. \qquad \text{(C7)}$$

For uncorrelated baths, each bath mode couples to only one site n, so that $g_{mk}g_{nk} = 0$ if $m \neq n$. If we let n_k be the index of the site to which mode k couples and let $g_k \equiv g_{nk}$, then

$$\xi_k = \left(1-\left(\frac{1+2\bar{n}(\Omega_k)}{\Omega_k}\right)\frac{\sum_\kappa e^{-\beta\hbar\tilde{\omega}_\kappa}u_{\kappa n_k}\sum_m u_{\kappa m}\tilde{V}_{mn_k}}{\sum_\kappa e^{-\beta\hbar\tilde{\omega}_\kappa}u_{\kappa n_k}^2}\right)^{-1}. \qquad \text{(C8)}$$

Numerically, this self-consistency condition can be solved by preparing an intial guess for the ξ_k coefficients (e.g., $\xi_k = 1$), and then iteratively calculating the quantity on the right hand side of Eq. (C8), each time replacing the ξ_k coefficients from the last round with the new calculated values from the right-hand side of Eq. (C8). For all spectra calculated in this work, this refinement was considered converged with then root-mean-square deviation between the left- and right-hand sides of Eq. (C8) was less than 10^{-10} across a discretely sampled frequency axis extending from -5000 to +5000 cm^{-1} with a step size of 1 cm^{-1}. (Since the ξ_k coefficients are uniformly zero for negative frequencies, this corresponds to a positive-frequency tolerance of $2\cdot10^{-10}$).

Note that two simple limits emerge naturally from this expression: when $\Omega_k \to 0$, the $\frac{1}{\Omega_k}$ term on the right-hand-side of Eq. (C8) causes the $\left(\frac{1+2\bar{n}(\Omega_k)}{\Omega_k}\right)$ term to diverge, so that $\xi_k \to 0$. Conversely, when $\Omega_k \to \infty$, this term approaches zero, and $\xi_k \to 1$.

Appendix D: Numerical Simulations

Fluorescence spectra were calculated in the VPT method following Eq. (51) under the assumption of uncorrelated baths described in Section II E. Numerical calculations were implemented in Jupyter Notebooks using the Python language. For spectra depicted Figures 3 and 4, static disorder was included in the form of an uncorrelated Gaussian site energy distribution with $\sigma = 100$ cm^{-1} for each pigment. In dimer simulations, averaging was performed numerically by first explicitly calculating line shapes for 30 distinct values of the inter-dimer splitting ω_{12}, covering a range from $\omega_{12} = 0$ to $\frac{\omega_{12}}{2\pi c} = 600$ cm^{-1}. (Since all monomers are assumed identical apart from the site energy, line shapes for ω_{12} and $-\omega_{12}$ are identical.) These separate spectra were then averaged together, including a normal-distribution weighting factor for a Gaussian with standard deviation 2σ. (The factor of 2 accounts for the fact that, for uncorrelated site energies, the ω_{12} distribution function is twice as broad as the distribution function for ω_1 and ω_2 separately.) Finally, this explicitly averaged spectrum was convolved with a Gaussian profile with standard deviation $\frac{\sigma}{2}$ to account for the variation of the mean frequency $\frac{\omega_1+\omega_2}{2}$. See Ref.[23] for further details on this procedure.

Calculations were carried out using two different sets of model parameters:

1. WSCP Parameters

Simulations reported in all figures *other than* Figure 2 use parameters intended to mimic as closely as possible experimental results for the WSCP complex. (Unless otherwise noted, system-bath interactions are assumed to be identical for WT LvWSCP, WT CaWSCP, and the Q57K LvWSCP mutant.) For the continuous phonon density, we use the log-normal fit reported in Ref.[45] to the experimental ΔFLN spectrum of Ref.[44] For the higher-frequency discrete mode density, we use a reparameterized density that (starting from the WT CaWSCP density of Ref.[44]) is optimized against the 77 K fluorescence spectrum of the Q57K LvWSCP mutant. Details on this procedure and the resulting HR values are reported in Ref.[23] Line shape functions for all spectra calculated using WSCP parameters were multiplied by an exponential decay with a decay constant of $\tau = 10$ ps to provide a finite linewidth to the single-site spectra in the frequency domain.

Frequency, cm^{-1}	HR factor
11.38	0.0263
15.78	0.0263
19.67	0.0263
23.44	0.0263
27.25	0.0263
31.19	0.0263
35.35	0.0263
39.81	0.0263
44.65	0.0263
50.00	0.0263
55.99	0.0263
62.81	0.0263
70.73	0.0263
80.16	0.0263
91.75	0.0263
106.64	0.0263
127.08	0.0263
158.45	0.0263
219.73	0.0263
90.26	0.0502
256.13	0.0112
360.12	0.0255
500.00	0.0173
747.01	0.0344
1000.00	0.0467
1192.74	0.0863
1348.04	0.0254
1533.51	0.0389
1684.01	0.0062

TABLE I. Discrete representation of CP29 spectral density.

2. CP29 Parameters

For the numerical benchmarking results described in Figure 2, we use a simplified spectral density with a smaller number of discrete vibrations. This choice is made to ensure convergence of the explicit matrix-diagonalization calculations, for which numerical cost scales quickly with both increases in the number of modes and the overall system-bath coupling strength. The spectral density is represented with 29 vibrational modes mimicking the ΔFLN line shape of the CP29 complex.[51] The low-frequency PSB was fitted with 19 discrete modes in Ref.[7]. Positions and HR factors of 10 modes representing the high-frequency spectrum were optimized by a fit to the 39 local modes of CP29. The resulting set of vibrations utilized both in numerical and VPT modeling shown in Fig.2 is summarized in Table I.

Numerical simulations were conducted in the home-built Python code that constructs Hamiltonian of eq 1 in a vibrational basis, while truncating vibrational quanta

of each pigment's normal mode based on their estimated intensity. The intensity of each electronic-vibrational state is determined using HR factors and populations, in the approximation that all vibrational modes are assigned to a single chromophore. The intensity cut-off of 10^{-8} utilized in this work ensures that the fluorescence spectra in Fig. 2 are converged within a line thickness. The T = 0 K fluorescence lineshape is obtained by finding the lowest energy state and its eigenvector of the vibronic Hamiltonian using the iterative Lanczos diagonalization.

[1] T. Renger and R. A. Marcus, "On the relation of protein dynamics and exciton relaxation in pigment–protein complexes: An estimation of the spectral density and a theory for the calculation of optical spectra," The Journal of Chemical Physics **116**, 9997–10019 (2002), https://pubs.aip.org/aip/jcp/article-pdf/116/22/9997/19069521/9997_1_online.pdf.

[2] V. I. Novoderezhkin, M. A. Palacios, H. van Amerongen, and R. van Grondelle, "Energy-transfer dynamics in the lhcii complex of higher plants: Modified redfield approach," The Journal of Physical Chemistry B **108**, 10363–10375 (2004), https://doi.org/10.1021/jp0496001.

[3] V. Tiwari, W. K. Peters, and D. M. Jonas, "Electronic resonance with anticorrelated pigment vibrations drives photosynthetic energy transfer outside the adiabatic framework," Proc. Natl. Acad. Sci. **110**, 1203–1208 (2012).

[4] F. D. Fuller, J. Pan, S. S. S. Andrius Gelzinis, Vytautas Butkus, D. E. Wilcox, C. F. Yocum, L. Valkunas, D. Abramavicius, and J. P. Ogilvie, "Vibronic coherence in oxygenic photosynthesis," Nature Chem **6**, 706–711 (2014).

[5] D. M. Jonas, "Vibrational and nonadiabatic coherence in 2d electronic spectroscopy, the jahn–teller effect, and energy transfer," Annual Review of Physical Chemistry **69**, 327–352 (2018).

[6] N. J. Hestand and F. C. Spano, "Expanded theory of h- and j-molecular aggregates: The effects of vibronic coupling and intermolecular charge transfer," Chemical Reviews **118**, 7069–7163 (2018), pMID: 29664617.

[7] M. Reppert, "Delocalization effects in chlorophyll fluorescence: Nonperturbative line shape analysis of a vibronically coupled dimer," The Journal of Physical Chemistry B **124**, 10024–10033 (2020), pMID: 33138372, https://doi.org/10.1021/acs.jpcb.0c05789.

[8] J. Cao and R. J. Silbey, "Optimization of exciton trapping in energy transfer processes," The Journal of Physical Chemistry A **113**, 13825–13838 (2009), pMID: 19929005, https://doi.org/10.1021/jp9032589.

[9] A. Ishizaki and G. R. Fleming, "On the adequacy of the redfield equation and related approaches to the study of quantum dynamics in electronic energy transfer," J. Chem. Phys. **130**, 234110 (2009), https://doi.org/10.1063/1.3155214.

[10] G. D. Scholes, G. R. Fleming, A. Olaya-Castro, and R. van Grondelle, "Lessons from nature about solar light harvesting," Nature Chemistry **3**, 763–774 (2011).

[11] A. Chenu and G. D. Scholes, "Coherence in energy transfer and photosynthesis," Annual Review of Physical Chemistry **66**, 69–96 (2015).

[12] T. Renger and F. Müh, "Understanding photosynthetic light-harvesting: a bottom up theoretical approach," Phys. Chem. Chem. Phys. **15**, 3348–3371 (2013).

[13] J. Ma and J. Cao, "Förster resonance energy transfer, absorption and emission spectra in multichromophoric systems. I. Full cumulant expansions and system-bath entanglement," The Journal of Chemical Physics **142**, 094106 (2015), https://pubs.aip.org/aip/jcp/article-pdf/doi/10.1063/1.4908599/13811273/094106_1_online.pdf.

[14] E. N. Zimanyi and R. J. Silbey, "Theoretical description of quantum effects in multi-chromophoric aggregates," Philosophical Transactions of the Royal Society A: Mathematical, Physical and Engineering Sciences **370**, 3620–3637 (2012), https://royalsocietypublishing.org/doi/pdf/10.1098/rsta.2011.0204.

[15] S. J. Jang, "Partially polaron-transformed quantum master equation for exciton and charge transport dynamics," The Journal of Chemical Physics **157**, 104107 (2022), https://pubs.aip.org/aip/jcp/article-pdf/doi/10.1063/5.0106546/16549492/104107_1_online.pdf.

[16] A. Srivastava, S. Ahad, J. H. Wat, and M. Reppert, "Accurate prediction of mutation-induced frequency shifts in chlorophyll proteins with a simple electrostatic model," J. Chem. Phys. **155** (2021), 10.1063/5.0064567.

[17] D. D. Bednarczyk, D. O. Dym, D. V. Prabahar, D. Y. Peleg, D. H. Pike, and D. D. Noy, "Fine Tuning of Chlorophyll Spectra by Protein-Induced Ring Deformation," Angew. Chem. **55**, 6901–6905 (2016).

[18] A. Agostini, E. Meneghin, L. Gewehr, D. Pedron, D. M. Palm, D. Carbonera, H. Paulsen, E. Jaenicke, and E. Collini, "How water-mediated hydrogen bonds affect chlorophyll a/b selectivity in water-soluble chlorophyll protein," Scientific Reports **9**, 18255 (2019).

[19] R. G. Saer, V. Stadnytskyi, N. C. Magdaong, C. Goodson, S. Savikhin, and R. E. Blankenship, "Probing the excitonic landscape of the chlorobaculum tepidum fenna-matthews-olson (fmo) complex: a mutagenesis approach," Biochim. Biophys. Acta (BBA) - Bioenergetics **1858**, 288 – 296 (2017).

[20] R. Saer, G. S. Orf, X. Lu, H. Zhang, M. J. Cuneo, D. A. Myles, and R. E. Blankenship, "Perturbation of bacteriochlorophyll molecules in fenna–matthews–olson protein complexes through mutagenesis of cysteine residues," Biochimica et Biophysica Acta (BBA) - Bioenergetics **1857**, 1455–1463 (2016).

[21] G. S. Orf, R. G. Saer, D. M. Niedzwiedzki, H. Zhang, C. L. McIntosh, J. W. Schultz, L. M. Mirica, and R. E. Blankenship, "Evidence for a cysteine-mediated mechanism of excitation energy regulation in a photosynthetic antenna complex," Proceedings of the National Academy of Sciences **113**, E4486–E4493 (2016), https://www.pnas.org/doi/pdf/10.1073/pnas.1603330113.

[22] N. M. Ennist, S. Wang, M. A. Kennedy, M. Curti, G. A. Sutherland, C. Vasilev, R. L. Redler, V. Maffeis, S. Shareef, A. V. Sica, A. S. Hua, A. P. Deshmukh, A. P. Moyer, D. R. Hicks, A. Z. Swartz, R. A. Cacho, N. Novy, A. K. Bera, A. Kang, B. Sankaran, M. P. Johnson, A. Phadkule, M. Reppert, D. Ekiert, G. Bhabha, L. Stewart, J. R. Caram, B. L. Stoddard, E. Romero, C. N. Hunter, and D. Baker, "De novo design of proteins housing excitonically coupled chlorophyll special pairs," Nature Chemical Biology (2024), 10.1038/s41589-024-01626-0.

[23] G. Grechishnikova, J. H. Wat, N. de Cordoba, E. Miyake, A. Phadkule, A. Srivastava, S. Savikhin, L. Slipchenko, L. Huang, and M. Reppert, "Controlling vibronic coupling in chlorophyll proteins: The effects of excitonic delocalization and vibrational localization," The Journal of Physical Chemistry Letters **15**, 9456–9465 (2024), pMID: 39250712, https://doi.org/10.1021/acs.jpclett.4c01826.

[24] C. Friedl, D. G. Fedorov, and T. Renger, "Towards a quantitative description of excitonic couplings in photosynthetic pigment–protein complexes: quantum chemistry driven multiscale approaches," Phys. Chem. Chem. Phys. **24**, 5014–5038 (2022).

[25] T. Renger, M. Madjet, A. Knorr, and F. Müh, "How the molecular structure determines the flow of excitation energy in plant light-harvesting complex ii," Journal of Plant Physiology **168**, 1497–1509 (2011), regulation of plant primary metabolism.

[26] E. Bloemsma, M. Silvis, A. Stradomska, and J. Knoester, "Vibronic effects and destruction of exciton coherence in optical spectra of j-aggregates: A variational polaron transformation approach," Chemical Physics **481**, 250–261 (2016), quantum Dynamics and Femtosecond Spectroscopy dedicated to Prof. Vladimir Y. Chernyak on the occasion of his 60th birthday.

[27] V. May and O. Kühn, *Charge and energy transfer dynamics in molecular systems* (John Wiley & Sons, 2023) Chap. 6.

[28] C. K. Lee, J. Moix, and J. Cao, "Accuracy of second order perturbation theory in the polaron and varia-

tional polaron frames," The Journal of Chemical Physics **136**, 204120 (2012), https://pubs.aip.org/aip/jcp/article-pdf/doi/10.1063/1.4722336/13889228/204120_1_online.pdf.

[29]R. A. Harris and R. Silbey, "Variational calculation of the tunneling system interacting with a heat bath. II. Dynamics of an asymmetric tunneling system," The Journal of Chemical Physics **83**, 1069–1074 (1985), https://pubs.aip.org/aip/jcp/article-pdf/83/3/1069/18954022/1069_1_online.pdf.

[30]M. Cho, H. M. Vaswani, T. Brixner, J. Stenger, and G. R. Fleming, "Exciton analysis in 2d electronic spectroscopy," The Journal of Physical Chemistry B **109**, 10542–10556 (2005).

[31]G. Renger, J. Pieper, C. Theiss, I. Trostmann, H. Paulsen, T. Renger, H. Eichler, and F.-J. Schmitt, "Water soluble chlorophyll binding protein of higher plants: A most suitable model system for basic analyses of pigment–pigment and pigment–protein interactions in chlorophyll protein complexes," Journal of Plant Physiology **168**, 1462–1472 (2011), regulation of plant primary metabolism.

[32]D. Horigome, H. Satoh, N. Itoh, K. Mitsunaga, I. Oonishi, A. Nakagawa, and A. Uchida, "Structural mechanism and photoprotective function of water-soluble chlorophyll-binding protein*," Journal of Biological Chemistry **282**, 6525–6531 (2007).

[33]T. Renger, I. Trostmann, C. Theiss, M. E. Madjet, M. Richter, H. Paulsen, H. J. Eichler, A. Knorr, and G. Renger, "Refinement of a structural model of a pigment-protein complex by accurate optical line shape theory and experiments," The Journal of Physical Chemistry B **111**, 10487–10501 (2007), pMID: 17696386.

[34]S. Ahad, C. Lin, and M. E. Reppert, "Photosynthetic protein spectroscopy lab," (2020).

[35]S. Ahad, C. Lin, and M. Reppert, "PigmentHunter: A point-and-click application for automated chlorophyll-protein simulations," The Journal of Chemical Physics **160**, 154111 (2024), https://pubs.aip.org/aip/jcp/article-pdf/doi/10.1063/5.0198443/19889970/154111_1_5.0198443.pdf.

[36]M. E. Madjet, A. Abdurahman, and T. Renger, "Intermolecular coulomb couplings from ab initio electrostatic potentials: Application to optical transitions of strongly coupled pigments in photosynthetic antennae and reaction centers," The Journal of Physical Chemistry B **110**, 17268–17281 (2006), pMID: 16928026, https://doi.org/10.1021/jp0615398.

[37]F. J. Kleima, E. Hofmann, B. Gobets, I. H. van Stokkum, R. van Grondelle, K. Diederichs, and H. van Amerongen, "Förster excitation energy transfer in peridinin-chlorophyll-a-protein," Biophysical Journal **78**, 344–353 (2000).

[38]M. Linke, A. Lauer, T. von Haimberger, A. Zacarias, and K. Heyne, "Three-dimensional orientation of the qy electronic transition dipole moment within the chlorophyll a molecule determined by femtosecond polarization resolved vis pump-ir probe spectroscopy," Journal of the American Chemical Society **130**, 14904–14905 (2008), pMID: 18928259, https://doi.org/10.1021/ja804096s.

[39]A. Ishizaki and G. R. Fleming, "Unified treatment of quantum coherent and incoherent hopping dynamics in electronic energy transfer: Reduced hierarchy equation approach," J. Chem. Phys. **130**, 234111 (2009), https://doi.org/10.1063/1.3155372.

[40]H. Liu, L. Zhu, S. Bai, and Q. Shi, "Reduced quantum dynamics with arbitrary bath spectral densities: Hierarchical equations of motion based on several different bath decomposition schemes," The Journal of chemical physics **140** (2014).

[41]Z. Tang, X. Ouyang, Z. Gong, H. Wang, and J. Wu, "Extended hierarchy equation of motion for the spin-boson model," The Journal of Chemical Physics **143** (2015).

[42]T. Ikeda and G. D. Scholes, "Generalization of the hierarchical equations of motion theory for efficient calculations with arbitrary correlation functions," The Journal of chemical physics **152** (2020).

[43]S. Kundu and N. Makri, "PathSum: A C++ and Fortran suite of fully quantum mechanical real-time path integral methods for (multi-)system + bath dynamics," The Journal of Chemical Physics **158**, 224801 (2023), https://pubs.aip.org/aip/jcp/article-pdf/doi/10.1063/5.0151748/18281463/224801_1_5.0151748.pdf.

[44]J. Pieper, M. Rätsep, I. Trostmann, H. Paulsen, G. Renger, and A. Freiberg, "Excitonic energy level structure and pigment-protein interactions in the recombinant water-soluble chlorophyll protein. i. difference fluorescence line-narrowing," The Journal of Physical Chemistry B **115**, 4042–4052 (2011).

[45]A. Kell, X. Feng, M. Reppert, and R. Jankowiak, "On the shape of the phonon spectral density in photosynthetic complexes," The Journal of Physical Chemistry B **117**, 7317–7323 (2013).

[46]J. Adolphs, F. Maier, and T. Renger, "Wavelength-dependent exciton–vibrational coupling in the water-soluble chlorophyll binding protein revealed by multilevel theory of difference fluorescence line-narrowing," The Journal of Physical Chemistry B **122**, 8891–8899 (2018), pMID: 30183300, https://doi.org/10.1021/acs.jpcb.8b08410.

[47]M. Reppert, V. Naibo, and R. Jankowiak, "Accurate modeling of fluorescence line narrowing difference spectra: Direct measurement of the single-site fluorescence spectrum," The Journal of Chemical Physics **133**, 014506 (2010), https://pubs.aip.org/aip/jcp/article-pdf/doi/10.1063/1.3455890/16051661/014506_1_online.pdf.

[48]J. Pieper and A. Freiberg, "Electron–phonon and exciton–phonon coupling in light harvesting, insights from line-narrowing spectroscopies," in *The Biophysics of Photosynthesis*, edited by J. Golbeck and A. van der Est (Springer New York, New York, NY, 2014) pp. 45–77.

[49]M. Reppert, A. Kell, T. Pruitt, and R. Jankowiak, "Comments on the optical lineshape function: Application to transient hole-burned spectra of bacterial reaction centers," The Journal of Chemical Physics **142**, 094111 (2015), https://pubs.aip.org/aip/jcp/article-pdf/doi/10.1063/1.4913685/13811478/094111_1_online.pdf.

[50]M. Reppert, "Modeling of resonant hole-burning spectra in excitonically coupled systems: The effects of energy-transfer broadening," The Journal of Physical Chemistry Letters **2**, 2716–2721 (2011), https://doi.org/10.1021/jz2012353.

[51]M. Rätsep, J. Pieper, K.-D. Irrgang, and A. Freiberg, "Excitation wavelength-dependent electron-phonon and electron-vibrational coupling in the cp29 antenna complex of green plants," The Journal of Physical Chemistry B **112**, 110–118 (2008), https://doi.org/10.1021/jp075170d.